Journal of Materials Chemistry A

Accepted Manuscript

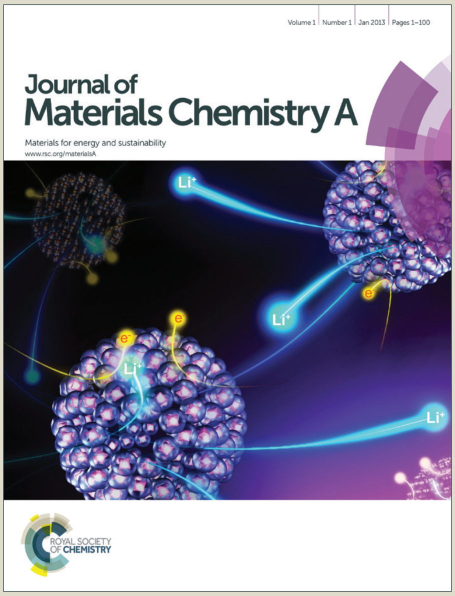

ROYAL SOCIETY OF CHEMISTRY

www.rsc.org/materialsA

Three Dimensional Architectures: Design, Assembly and Application in Electrochemical Capacitors

Minghao Yu,‡ Weitao Qiu,‡ Fuxin Wang, Teng Zhai, Pingping Fang, Xihong Lu* and Yexiang Tong*

MOE of the Key Laboratory of Bioinorganic and Synthetic Chemistry, KLGHEI of Environment and Energy Chemistry, School of Chemistry and Chemical Engineering, Sun Yat-Sen University, Guangzhou 510275, People's Republic of China.

E-mail: *luxh6@mail.sysu.edu.cn* (X. H. Lu); *chedhx@mail.sysu.edu.cn* (Y. X. Tong).

‡ *These authors contributed equally to this work.*

Abstract:

Currently, supercapacitors (SCs) are considered as one kind of the most promising energy storage devices, which mainly relies on their unique properties, such like high output power, long cycling stability, fast charge/discharge capability and so on. Nevertheless, the unsatisfied energy density of SCs still limits their wild promotion in practical applications. Given this, designing three dimensional (3D) architectures for SCs electrodes is perceived as an efficient strategy, since the well-constructed 3D structures could enable reduced "dead surface", good electron transport kinetics, hierarchical porous channels and short ionic diffusion distances. This review aims to describe the current progress of different synthetic processes for the preparation of 3D SCs electrodes, dividing into template-assisted strategy and non-template strategy. We summarize recently proposed methods, novel structures,

electrochemical performances for these 3D electrodes. Advantages and disadvantages accompanying them were also analyzed. Lastly, we further discussed the challenges and prospects of the fabrication of 3D SCs electrodes.

1. Introduction

To respond to the rapid growth of the global population and economy, there is ever-increasing demand for sustainable sources of energy.[1, 2] In view of the problems of climate change and limited availability of fossils, developing efficient renewable energy conversion and storage devices has attracted extensive interest.[3, 4] Substantial efforts have been devoted to the development of new technologies for harvesting renewable energies, such as wind, solar energy, geothermal energy, and tidal energy.[3-5] However, constructing highly efficient, low cost, and environmentally friendly energy storage devices to store these intermittent renewable energies remains one of the greatest challenges.[5] In this context, supercapacitors (SCs), also known as electrochemical capacitors, have been considered to be promising candidates for energy storage devices due to their high power density (> 10 kW/kg), fast charge/discharge capability (within seconds) and long cyclic stability (> 10^5 cycles).[6-9] Fig. 1 illustrates the power and energy densities of various types of energy storage systems. In comparison to conventional capacitors, SCs could deliver several orders of magnitude higher specific energy density due to their unique charge storage mechanisms, especially their pseudocapacitance. Meanwhile, faster discharge in a short period of time was accompanied with SCs, enabling much higher output power than batteries. All these features not only make SCs complement for batteries by providing back-up power supplies to deal with high power demands, but also enable them to be favorable power source for portable power tools, emergency power supplies and hybrid electric vehicles.

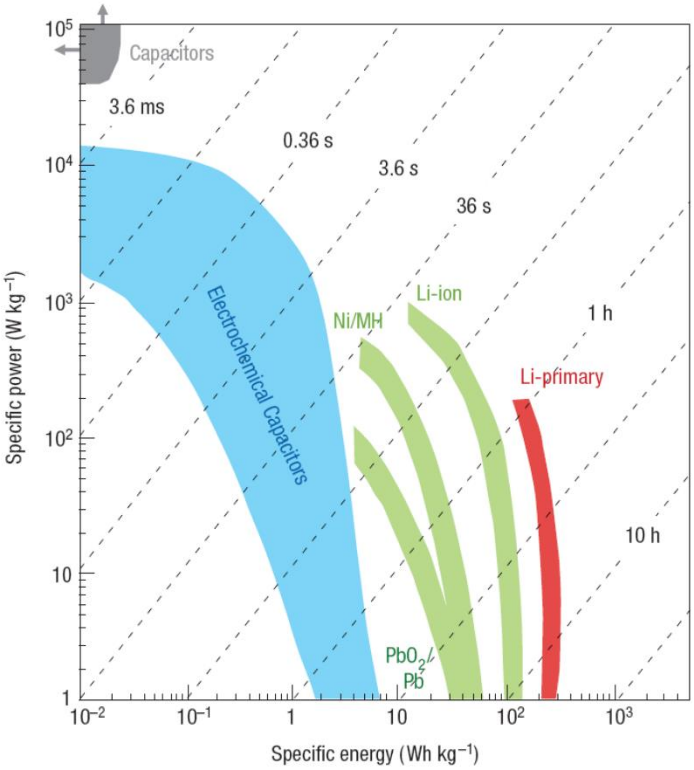

Fig. 1. Specific power density against specific energy density, also called a Ragone plot, for various electrical energy storage devices. Reproduced from Ref. [10] with permission from the Nature Publishing Group.

However, the main drawback of SCs that they are not capable of delivering enough large energy densities comparable to those of lithium ion batteries, severely hinders their practical application as primary power sources.[5, 11] It is imperative to further boost the energy density of SCs while maintain their high power density and long cyclic stability. Tremendous efforts have been devoted to this issue and great advances have been obtained in the latest ten years.[8, 9] The maximum energy (E) stored for a single cell SC is given in eqns (1):

$$E = \frac{1}{2}CV^2 \qquad (1)$$

where C is the total capacitance of the SC, while V is the operation potential window of the SC. Both of these two elements extensively depends upon the electrode materials, which is accordingly crucial to the final energy density of the as-fabricated SC. Up to now, the promising electrode materials can be generally categorized into (1) carbon material with large surface area; (2) transition metal compounds like metal oxides/hydroxides, metal nitrides, metal sulfides and so on; (3) conducting polymers. These materials own their natural pros and cons when used as capacitive electrodes.[6] For instance, carbon materials are evaluated as even commercial SC electrodes, in terms of their high conductivity and superior electrochemical stability. However, the insufficient specific capacitance only derived from electronic double layer capacitance severely limits their widespread generalization. Meanwhile, even though high specific capacitance can be obtained for both metal compounds and conducting polymers with the introduction of Faradic redox reaction, obvious demerits cannot be ignored for them like the poor conductivity for metal oxides and fast capacitance fade for conducting polymers. Combining different materials to construct composites is a new research direction in SC electrodes exploration, which realizes a synergistic effect of them through the design of various components.

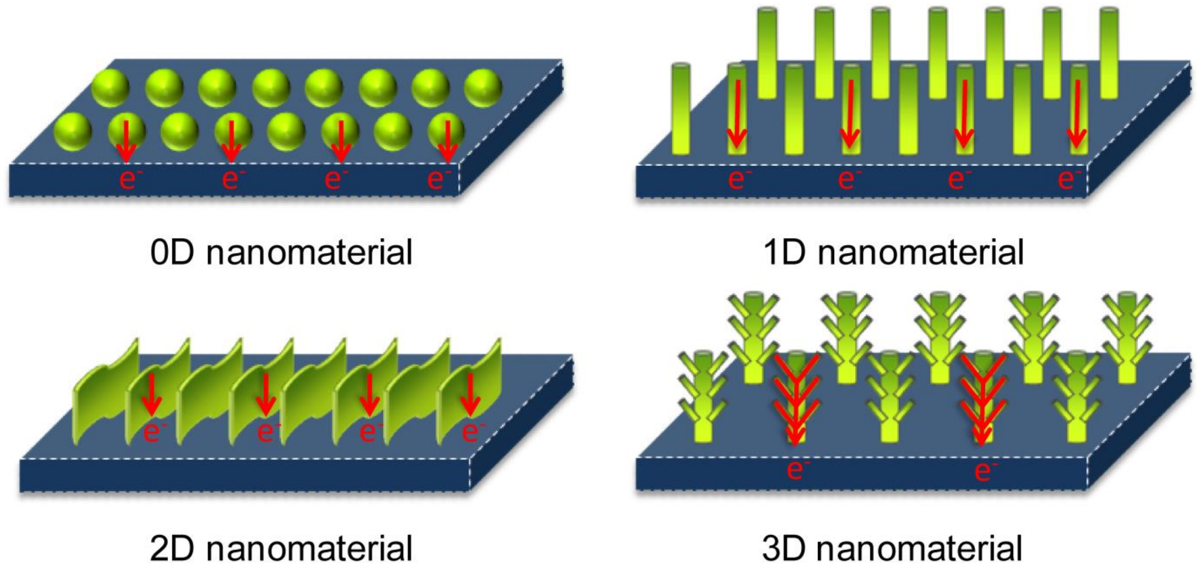

Fig. 2. Schematic illustration of the possible electron path taking place on different nano-designed electrodes with 0D, 1D, 2D, and 3D architectures.

Constructing nanostructured active materials is another feasible solution owing to the new and superb properties obtained at the nanoscale. The well-designed nanostructure can offer short ionic diffusion distance to the electrode surface, efficient transport pathway for electrons within the electrode, and more electroactive sites for electronic storage, hence resulting in both fast kinetics and high charge/discharge capacities even at high current densities.[6] According to their morphology, nanostructured materials can be generally classified into zero-dimensional (0D) nanomaterial (nanoparticles, nanospheres *etc.*), one-dimensional (1D) nanomaterial (nanorods, nanowires *etc.*), two-dimensional (2D) (nanoplates *etc.*) nanomaterial, and three-dimensional (3D) nanomaterial. Among them, 3D nanostructured electrodes attract particular interest when compared to other low dimensional structures.[12-15] As shown in Fig. 2, 3D constructed electrodes, which are hierarchically assembled from low-dimensional units (including one kind or more of 0D, 1D, 2D nanomaterials), not only can inherit the intrinsic properties of low-dimensional structure, but also enable faster and more efficient electronical transfer attributing to the multi-pathway formed from the structural interconnectivities. Moreover, 3D architectures always allow sufficient utilization of space, which are benefit for reducing "dead surface" without sacrifice of hierarchical porous channels. It also offer opportunities to the assembly of large mass loading electrodes with much enhanced energy storage capacity, if rationally designed nanostructure is chosen.

To date, large amounts of synthetic strategies for the fabrication of 3D SCs electrodes have been reported, numerous 3D electrodes with various structures have emerged. In this review, a brief summary of recent research progress on the development of these 3D electrodes is presented, mainly including template-assisted methods and none-template methods. The parameters related to the capacitive properties were addressed to illustrate the metric of the 3D architectures. As for these template-assisted methods, we categorically discuss the synthesis approaches and electrochemical applications in detail based on the template selected. The most common 3D templates include nickel foam, Silica with various morphologies, polystyrene spheres and some others. The characteristics of these templates are also addressed. Then, we further summarize the applied strategies for fabricating 3D electrodes using non-template methods and their SC applications, which are classified according to the types of active materials including carbon materials, metal oxides and other materials. Moreover, the main challenges and new trends in 3D electrodes development have also been proposed. We hope our review can guide important progress in developing advanced SCs electrodes with high energy storage capability.

2. Evaluation of supercapacitor electrodes.

Current evaluation techniques for a SC electrode mainly include cyclic voltammetry (CV), galvanostatic charge/discharge (GCD) and electrochemical impedance spectroscopy (EIS) methods.[6, 16] In general, the capacitances of the electrodes can be calculated from CV and GCD curves basing on the eqns (2) and (3), respectively:

$$C_m = \frac{Q}{\Delta V \cdot m} = \frac{S_{CV}}{2v \cdot \Delta V \cdot m} \qquad (2)$$

$$C_m = \frac{Q}{\Delta V \cdot m} = \frac{I \cdot \Delta t}{\Delta V \cdot m} \qquad (3)$$

where C_m (F/g) is the specific capacitance, Q (C) is the average charge during the charging and discharging process, ΔV (V) is the potential window, m (g) is the mass loading of active material, S_{CV} (AV)is the integrated area of the CV curve, v (V/s) is the scan rate in CV test, I (A) is the constant discharging current during the GCD test, and Δt (s) is the discharging time. Large specific capacitances are favorable for the electrodes, which are also directed to high energy density. Particularly, the capacitance retention of the electrode tested at a high scan rate or large discharge current always reflect the fast charge/discharge and large power output ability. Besides, there are also some other characteristics for the CV and GCD curves corresponding the capacitive behaviors of electrodes. For example, the symmetry of their shapes suggests the reversibility of the redox reactions during the charge/discharge processes, the Coulombic efficiencies give the information of effective availability for stored energy, the IR drops observed from the discharge curves are related to the internal resistance of the electrodes, *etc*.

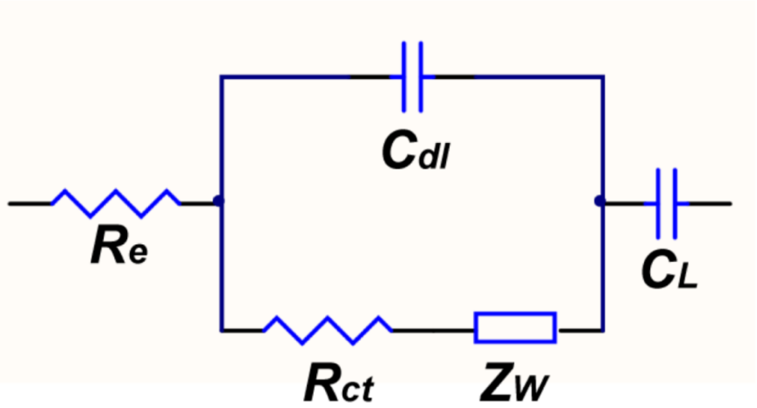

Fig. 3. The common equivalent circuit used to fit with the Nyquist plots.

As for the EIS measurement, Nyquist plots and Bode plots are most popular diagrams to assess the dynamic process of the electrode.[17] Nyquist plots provide the relationship between the imaginary part of impedance, *Z(f)''*, and the real part of impedance, *Z(f)'*, which usually consist of a single semicircle in the high-frequency region and a sloping line in the low-frequency region. Fitting with an equivalent circuit is a convenient method to analyze them as shown in Fig. 3. Among these parameters, charge transfer resistance (R_{ct}) implies the conductivity of the active material, which can also be obtained from the diameter of the semicircle at high frequency region. The pure capacitive feature could be determined by the impedance plots at low frequency range, which show a near vertical line to the real axis. However, in most of cases, the inclined angles of the line against the real axis are smaller than 90^o, corresponding to Warburg diffusion mechanism involved. In addition, Bode plots reflect the variation of the phase angle with increasing frequency, *f*. The purely capacitive behavior of the electrode corresponds to a closer phase angle to -90^o at low frequency. In particular, the frequency obtained at the phase angle of -45^o is a characteristic one, which corresponds to the frontier between the capacitive and resistive behavior of the electrode. A relaxation time τ_0 calculated from eqns (4), indicating the response time required to efficiently deliver the stored energy. Moreover, a capacitance is also calculated from eqns (5), which should be theoretically consistent with half of the total capacitance of the electrode.

$$\tau_0 = \frac{1}{f_0} \qquad (4)$$

$$C = \frac{1}{2\pi f_0 |Z(f_0)''|} \qquad (5)$$

3. Template-assisted fabrication of 3D electrodes

Template-assisted synthesis has been widely adopted to obtain certain structure inheriting original shape of the template scaffold. It is considered as the most straightforward method to contrive 3D structures with high uniformity, controllable pore size and tunable morphologies [18]. By various means like chemical vapor deposition (CVD), hydrothermal reaction and electrodeposition, multiple materials with different morphologies could grow on or bind with templates [19-21]. Therefore, active materials with particular structure could be loaded against the backbone, increasing electrode dimension and thus forming 3D network. Moreover, subsequent removal of templates will further generate pores and spacing, which could provide mass transfer pathway, ion diffusion buffer and extra surface area enabling effective contact with electrolyte. Enhancing effect of 3D electrodes might be attributed to the unique 3D structure with increased pore and surface area compared to the bulk counterparts [21, 22]. Versatile as template methods appear to be, the designing of 3D electrode seems to be contrarily limited by the various properties displayed by different templates, which should be consider at the very beginning of the design. In this section, three templates (nickel foams, silica templates and polystyrene spheres) and corresponding applications in SCs electrode fabrication will be mainly discussed due to the wide application of these three templates in building 3D SCs electrodes recently, while other template methods will be listed as the last part of the section for supplement.

3.1 Nickel foams

Nickel foam (NF), usually used as a 3D current collector, has a conductive and interconnected 3D skeleton of pure metal nickel. When serving as a 3D electrode template, such backbone features its high pore density (50-90%), excellent conductivity (350 S/cm), thermal stability, catalytic activity and susceptibility to acid etching (normally $FeCl_3$/HCl solution), which allows its selective removal after formation of active materials and leads to higher degree of electrode dimension. [23, 24] Due to the continuous network that NFs possess, electrodes produced by NF template method usually acquire monolithic structure. Recent researches on monolithic 3D electrodes for SCs application involving the application of NF were usually connected with a pre-coating of graphene layer to subsequently construct a composite of graphene foam and active materials (e.g. metal oxides or hydroxides), demonstrating high gravimetric or areal capacitance. In this perspective, graphene foam derived from NF templates will be mainly discussed as follow, accompanied with metal oxide/graphene foam composites and 3D electrodes using NFs as their own skeleton.

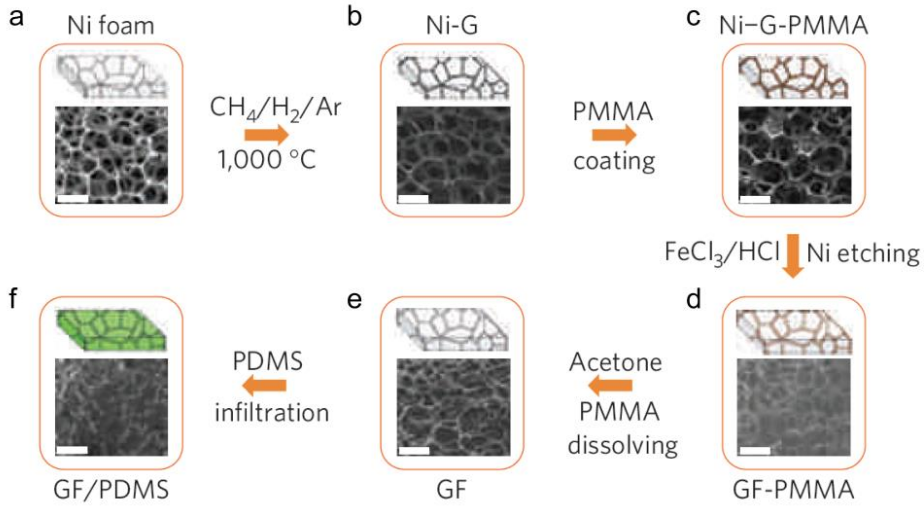

Fig. 4. (a-b) CVD growth of graphene films onto nickel foam in $CH_4/H_2/Ar$ atmosphere at 1000^{o}C. (c-d) Coating of PMMA as supporting layer along with the following nickel etching process in $FeCl_3/HCl$ solution. (e-f) Dissolution of PMMA layer and infiltration of PDMS support. Reproduced from Ref. [24] with permission from the Nature Publishing Group.

Graphene is one of the most common materials exploiting NF as template scaffold. To grow graphene layer on the network, CVD process was the first used method, in which the key to the successful deposition of graphene is the catalytic activity of NF, known as an important feature of nickel metal network. A representative synthesis procedure is shown in Fig. 4, which illustrates the preparation of the first reported 3D graphene foam derived from NF mold by Chen *et al*. [24] In this case, a defect-free graphene layer was initially deposited using catalysis-assisted CVD process in $CH_4/H_2/Ar$ atmosphere, followed by the impregnation of poly-(methyl methacrylate) (PMMA) to reinforce the strength of the graphene coating (Fig. 4a and b). Then, subsequent removal of nickel in $FeCl_3/HCl$ solution results in a self-supported graphene foam, of which the structure remained intact due to the PMMA layer (Fig. 4c and d). Finally, PMMA layer was dissolved and poly-(dimethyl siloxane) (PDMS) was infiltrated into the graphene framework to further strengthen the network to enhance flexibility (Fig. 4e and f). The resultant graphene network inherited 3D structure of NF with light density of 5 mg/cm^3, exhibiting high electron transfer efficiency due to the defect-free and continuous graphene produced by CVD method.

Due to its excellent conductivity and electrochemical performance, graphene foam prepared from NF template makes itself well eligible for electrode materials support. Thereby, plenty of researches on metal oxides/graphene foam composites emerged and their utilization for significant improvements of capacitance were well-known since then. [25-27] Growth of metal oxides like Co_3O_4 was examined by Dong *et al.* through simply immersing graphene framework into growth solution for hydrothermal reaction. [25] The as-obtained composite gave a capacitance of 1100 F/g at a current density of 10 A g^{-1}. He *et al.* [26] also reported a MnO_2-coated freestanding 3D graphene foam fabricated by square-wave pulse current electrodeposition of uniform MnO_2 coating on 3D graphene foam, showing a remarkable areal capacitance of 1.42 F/cm^2 with a high mass loading (92.9% of the whole electrode weight). Based on the CVD-derived graphene foam with macroscopic scaffold, constructing microscopic structure against its surface thereby produced a monolithic electrode with hierarchical structure that enhanced both electron and ion transfer efficiency of the active materials grown on the skeleton. For this purpose, He and his coworkers [28] also fabricated a 3D micro/nano-interconnected carbon based electrode comprising NF-derived graphene foam as its primary backbone, an outer layer of carbon nanotubes (CNTs) as the secondary and MnO_2 nanosheets attached on CNTs the third. After the growth of CNTs and MnO_2 thin layer, the electrode maintained the flexibility of NF-derived graphene foam and exhibited specific capacitance of 946 F/g, with mass loading of 0.1 mg/cm^2, well exceeding that of MnO_2/graphene foam electrode (482 F/g), a control sample without CNT forest. The result unraveled that the surface coating of CNTs nanostructure contributed to serve as conducting support as well as to extend the accessible or exposed area of MnO_2 nanosheets. Meanwhile, macro-pores of the primary scaffold allowed fast infiltration of electrolyte and therefore such hierarchical system achieved outstanding performance. Besides MnO_2/CNTs/graphene hybrids, microscopic honeycomb-like $CoMoO_4$ layers were assembled against the graphene foam surface in the same pursuit to extend the porous structure from macroscopic network to microscopic level by Yu and his group. [29] Similarly, extraordinary specific capacitance was demonstrated, with a monolithic electrode giving capacitance as high as 2741 F/g at a current density of 1.43 A/g and a remarkable capacitance retention of 96.36% at 400 A/g after 100000 cycles (electrode mass loading: 0.51 mg/cm^2). All these examples well substantiate that 3D conducting scaffolds with hierarchical structures are able to maximize the utilization of active materials and thus the capacitance and stability. [30, 31]

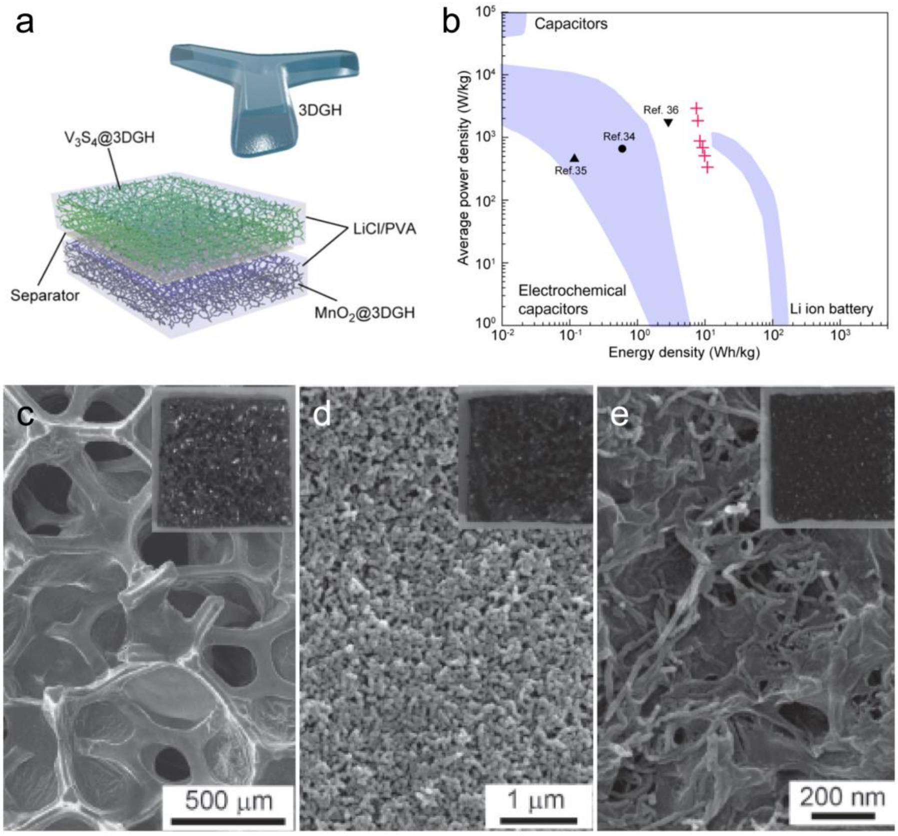

Fig. 5. (a) Illustration of V_3S_4/3DGH//MnO_2/3DGH all-quasi device. (b) Ragone plot of V_3S_4/3DGH//MnO_2/3DGH device, showing an energy density closing up to that of lithium ion batteries. (c) SEM image of ERGO electrode (d) SEM image of MnO_2-ERGO electrode (e) SEM image of CNT-ERGO electrode. Insets show the corresponding photograph of different electrodes. (a-b) Reproduced from Ref.[32] with permission from American Chemical Society and (c-e) from Ref. [33] with permission WILEY-VCH Verlag GmbH & Co. KGaA, Weinheim.

As CVD assisted fabrication is not the only way toward NF-derived 3D graphene foam, hydrothermal reduction of graphene oxide suspension was also conducted to assemble graphene on NF. [34] Zhai *et al.* [32] most recently fabricated NF-derived graphene foams (denoted as 3D graphene hollow structure, 3DGH) via a hydrothermal process without the need of PMMA impregnation. After annealing the as-prepared 3DGH in a reducing atmosphere, good crystallinity and conductivity were achieved and coating of MnO_2 layer and V_3S_4 onto 3DGH was followed with resultant electrodes denoted as MnO_2 /3DGH and V_3S_4/3DGH, respectively. Nyquist plot of the 3DGH was studied before and after nickel removal, indicating a charge transfer resistance of 0.3 Ω before and 1 Ω after nickel removal and no apparent electrical resistance change was observed. A quasi-solid state device, MnO_2/3DGH//V_3S_4/3DGH, was assembled with separator and gel electrolyte, in which the mass of active materials took up 24% of the whole capacitor (21 mg/cm^2 for whole device, Fig. 5a). As shown in Fig. 5b, the device delivered an extraordinary energy density with value of 7.4 Wh/kg at power density of 3000 W/kg, approaching up to Li-ion batteries. Other than hydrothermal fabrication, a facile and scalable electrochemical fabrication method is reported by Zhang *et al*.. [33] Graphene oxide was first casted onto NF framework via a solution process and an electrochemical reduction to induce electrochemically reduced graphene oxide (ERGO) on the surface of the skeleton to obtain ERGO electrodes (Fig. 5c). More interestingly, further research showed that MnO_2 were able to be attached on nickel backbone by simply coupling the electrochemical reduction with electrodeposition (Fig. 5d), while a facile dip-coating with subsequent electrochemical reduction realized the assembly of CNTs on ERGO foam surface (Fig. 5e). Both the MnO_2-ERGO and CNT-ERGO electrodes were inspected for SCs application at a current density of 1 A g^{-1}, showing a specific capacitance of 422.5 F/g and 280.4 F/g, respectively. EIS curves of MnO_2 ERGO, CNT–ERGO and ERGO showed that the equivalent series resistances (ESRs) of the three electrodes are very close, with value of 11, 9 and 5 Ω, respectively, inferring that those 3D frameworks of ERGO can serve as highly conductive backbones. Prolonged cycling stability was also achieved for those electrodes. The excellent performance further proved the importance of 3D network for SCs electrode and such skeleton granted the electrode superior flexibility while maintaining over 95% of its capacity after being bent into large angle for100 times.

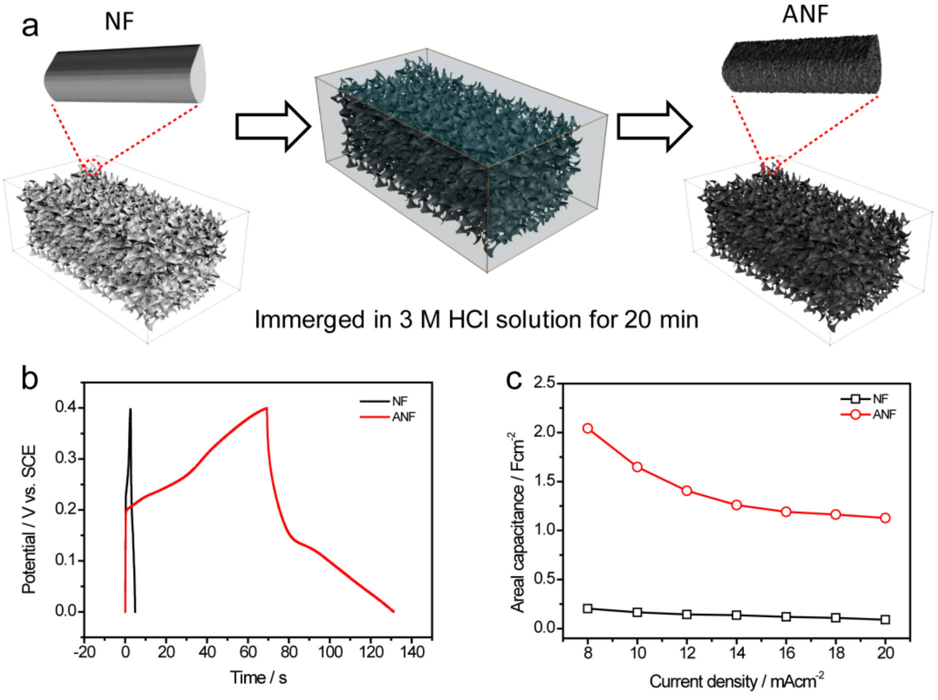

Fig. 6. (a) Schematic diagram illustrating the activation process of the NF, resultant ANF was darkened due to the activation. (b) Galvanostatic charge/discharge curves of the NF and ANF electrodes. (c) Areal capacitance as a function of the current density of the NF and ANF electrodes. Reproduced from Ref. [23] with permission from the Nature Publishing Group.

Despite the merits brought by template removal, NFs templates, in many cases, were remained after the coating of active materials, serving as a current collector as well as a 3D scaffold. [35-37] Graphene is costly and NF itself can serve as a conducting pathway when skipping template removal. [38] Moreover, vulnerable is nickel to the etching process and that enables itself as nickel source for in-situ growth of nickel oxides or hydroxides. [23, 39, 40] Under this consideration, other cases, which were in pursuit of scalable 3D electrode synthesis, used NF directly as conducting backbone without graphene coating. For instance, Yu *et al.* [23] developed a scale-up surface treatment for NF activation (activated nickel foam, namely ANF) to grow a layer of NiO on nickel network. Through partial etching of NF in the present of HCl, the original layer of NiO existing on NF surface was removed and a new layer of oxide was produced on the rougher surface (as shown in Fig. 6a) during drying process, giving an areal capacitance of 2.0 F/cm^2 at a current density of 8 mA/cm^2. An activated surface gave ANF superior surface capacitance compared to pristine NF (Fig. 6b) and excellent electrochemical performance was achieved at various current density (Fig. 6c). This work in fact was an example of in-situ growth of microscopic structure onto a macroporous nickel skeleton, in which NF was nickel source as well as a monolithic conductive support for producing an intact electrode at once. Another in-situ synthesis from NF was developed by Xiong *et al.*. [39] NiO layer of NF was first etch away and the foam was stored in a glass vial to allow surface oxidation in wet environment that formed a dense layer of $Ni(OH)_2$, followed by a alkaline and oxidative solution treatment to transform morphology into nanosheets array. After the transformation process, the dense layer still retained a high mass loading of 1.8-2.0 mg/cm^2. The as-obtained 3D nanosheets/NF electrode demonstrated specific capacitance of 2384.3 F/g at current density of 1 A/g.

In order to produce 3DNF electrode maintaining NF backbone, other ex-situ synthesis method of active materials on NF were also intensively investigated in recent publications. Primarily, these efforts involved simple and one-pot hydrothermal reaction and electrodeposition to obtain cost-effective and scalable 3D electrodes from NF templates. Metal oxides, [41-44] sulfides, [45, 46] hydroxides [36, 38] and their composites [35, 37, 47] with various morphologies were studied for their electrochemical performance and applications in SCs. For instance, several reports pertaining $NiCo_2O_4$ showed good prospects for application of such mixed metal oxide [41, 48]. Yuan *et al.* [49] synthesized mesoporous $NiCo_2O_4$ nanosheets on NF for 3D SCs electrodes, delivering specific capacitance of 1450 F/g at 20 A/g, with a relatively small active materials loading of 0.4 mg/cm^2. 3D metal oxide composites were also obtained directly through one-step hydrothermal route. Most recently, $NiCo_2O_4/MnO_2$ nanowire arrays on NF were shown by Zou *et al.*, [50] giving a specific capacitance of 2339 F/g at current density of 20 mA/cm^2. Through sulfidation of aforementioned $NiCo_2O_4$ in Na_2S solution, the resulted $NiCo_2S_4$ showed lower R_{ct} after sulfidation and achieved a capacitance of 2415 F/g at current density of 30 mA/cm^2, as demonstrated by Li *et al.*. [51] All those works had proved that facile preparation of high performance 3D electrodes for SCs is feasible by directly applying NF as supports.

3.2 Silica templates

Silica with various morphologies have been synthesized, such as nanoparticles, [52-54] nanosheets[55] and ordered mesoporous/macroporous structure[56-58]. Unlike NF templates, silica is much more stable against high temperature and acid solution. Thus, preparation method involving silica templates usually accompanied with high temperature or strong acid surroundings. [59] The highly stable structure of silica prevents the shrinkage of materials upon annealing or reaction, [60] while such stability in turn becomes a drawback of its application because of the difficult removal of silica templates (involving HF or hot base etching), limiting its use mainly within the field of carbonization of organic precursor to produce porous carbon network (e.g. ordered mesoporous carbon) or the preparation of stable materials against strong bases. [61-64] Nonetheless, silica templates with microscopic structure, such as particle-like and mesoporous structure introduce micro/meso-pores into target framework and thus broaden its potential application in building 3D electrodes.

Silica particle is one of the most commonly used silica templates, with advantages like facile preparation, controllable particle size and easy dispersion in solution[53, 54]. When used as templates, silica particles were dispersed in reaction solution first, followed by a growth process to coat active materials against the templates. The general preparation route might consist of three steps: 1) impregnation of active materials or precursor into the templates matrices; 2) pyrolysis or further treatment to achieve desired product with sufficient crystallinity; 3) removal of silica templates in HF solution or hot bases. For instance, Yu *el al.* [18] synthesized mesoporous $Li_4Ti_5O_{12}$ hollow spheres for lithium ion batteries (as shown in Fig. 7) showing excellent rate capability and cyclic stability. Typically, silica nanoparticles were initially dispersed in hydroxypropyl-cellulose/ethanol/water mixture to form a monodisperse colloid. Afterwards, TBOT was injected into the mixture to deposit TiO_2 layer against the silica templates. The following hydrothermal treatment in LiOH solution helped gradual removal of silica and meanwhile converted the TiO_2 coating into a precursor that was thereafter calcined in air to acquire discrete $Li_4Ti_5O_{12}$ hollow spheres. However, templates like silica particles without interconnected skeleton usually produced porous or hollow 3D structure in microscope, rather than a monolithic framework derived from NF. [65-67] The powdered product needed to be applied on Cu foil or Al foils before electrochemical investigation and the disruption of long-range electron transfer due to the disconnected nature of particles will hinder the capacitive performance by intercepting electrons during particle-to-particle transferring process.

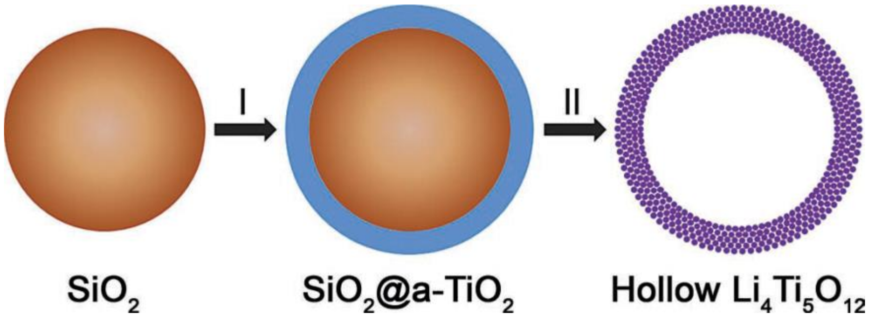

Fig. 7. Schematic illustration of $Li_4Ti_5O_{12}$ hollow spheres as a representative synthesis procedure using silica templates. Reproduced from Ref. [18] with permission from WILEY-VCH Verlag GmbH & Co. KGaA, Weinheim

In spite of monodisperse characteristic that silica particle features, efforts have been paid for silica-template fabrication of 3D structure that is continuous at a larger scope through assembling and fastening silica particles into a so-called 3D colloidal crystal. [68-71]Such fabrication methods involve precipitation of colloidal particle templates by external force like gravity, assembly process directed by capillary forces, electrostatic forces or hydrophobic interactions at oil–water interfaces and, finally, an optional fastening process through heating (especially for silica templates or polymer templates). [20] Once connections between particles were formed, a 3D network was obtained and active material can be confined in the spacing to cast out an inverse structure with interwoven network. As an example shown in Fig. 8, Wen *et al.* [72] attempted to build up a three-dimensional hierarchical porous carbon (3DHPC) by adopting preheated silica spheres that had formed necks between each other (Fig. 8a). Subsequent impregnation of order mesoporous carbon precursor (consisting of phenol, formaldehyde, NaOH and F127 surfactant) and a follow-up heat treatment gave rise to the formation of ordered mesoporous carbon in the spacing that existed between silica particle s(Fig. 8b and c). The as-prepared 3DHPC electrodes (mass loading ~ 5.5 mg/cm^2) were tested for capacitive deionization, showing a relatively low capacitance of 118.1 F/g which was however larger than that of regular ordered mesoporous carbon. Enhancements in IR drop and charge transfer resistance were also observed, revealing that an interconnected work might have an impact on electron transfer efficiency.

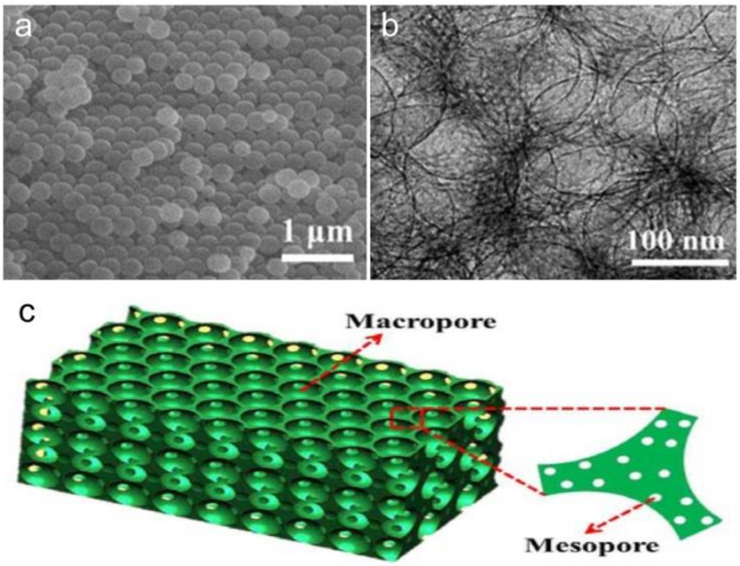

Fig. 8. (a) SEM image of periodically arranged PS colloidal crystal. (b) High magnification TEM image of 3DHPC electrode. (c) Illustration of bi-modal porous 3D structure of 3DHPC. Reproduced from Ref. [72].

The connected silica casting mold shows an interconnected network at relatively larger scope, but it is still much smaller than that of NF because of the limited size of silica particle. Besides, the preparation of colloidal crystal still required costly and time-consuming process. Therefore, more researches focused on fabricating 3D electrodes with template method that chose silica templates as an auxiliary tool to integrate meso-pores into macroporous skeleton (e.g. graphene foam or aerogel), building bi-modal or tri-modal porous 3D frameworks. [57, 73] Through combining graphene aerogel (GA) and mesoporous silica layer, a composite of graphene aerogel and mesoporous silica (denoted as GA-SiO_2) was successfully synthesized and exploited as a 3D electrode template by Wu and his coworkers, [74] as shown in Fig. 9a. In this case, a graphene aerogel was prepared from a hydrothermal reduction of graphene oxide dispersion and suspended in cetyltrimethylammonium bromide (CTAB) aqueous solution afterwards. The absorption of CTAB facilitated the uniform hydrolysis of tetraethoxysilane (TEOS) and thus produced even SiO_2 layer on GA surface. 3D GA-based mesoporous carbon (GA-MS) or GA-based metal oxides (GA-Co_3O_4, GA-RuO_2) were constructed via a nanocasting technology. To prove that the GA-SiO_2 was competent to serve as a versatile 3D electrode backbone for SCs, the as-fabricated GA-MS and GA-RuO_2 were evaluated in 1 M H_2SO_4 electrolyte, giving specific capacitance of 226 F g^{-1} at 1 mV s^{-1} and 560 F/g at 5 mV s^{-1}, separately. Further calculation of pseudocapacitive utilization of RuO_2 (1090 F/g) showed that the 3D GA-SiO_2 templates had a large accessible electrode-electrolyte interface due to the bi-modal porous structure. Besides building silica layer on the backbone surface to increase porosity, silica can be intercalated into macroporous framework to prevent restacking and induce hierarchical structure as well. One of these examples was shown by Lei *et al.*, [73] in which they attempted to infiltrate mesoporous silica spheres into graphene stacks as templates to induce intercalated mesoporous carbon sphere via CVD, depositing carbon inside the meso-pores of those intercalated silica spheres. The resultant carbon spheres after removal of silica remain intact and intercalated in the graphene matrices, preventing the restacking of graphene without impeding the electron conduction of the framework (Fig. 9b, 9c). The composites that were subsequently submitted to NH_3 atmosphere for reduction gave outstanding capacity retention which remained 85% of the initial compared with less than 30% retention for pristine RGO electrode (Fig. 9d). The result revealed that the enhanced rate performance could be ascribed to the presence of highly conductive reduced graphene sheets as well as the intercalated mesoporous carbon spheres, which served as conducting spacers.

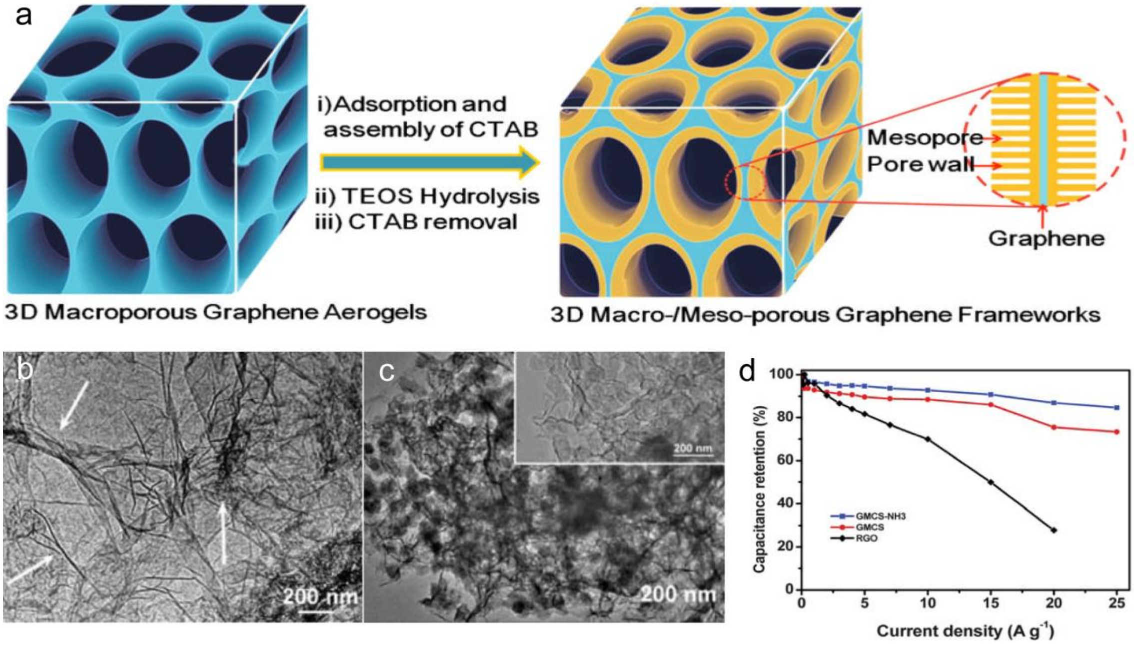

Fig. 9. (a) Schematic illustration of the fabrication of hierarchical macro- and mesoporous GA-SiO_2 frameworks. (b) TEM image of RGO. (c) TEM image of GMCS. (d) Capacitance

retention against current density of RGO and GMCS-based electrodes. Reproduced from Ref. [177] with permission from American Chemical Society and Ref. [74].

3.3 Polystyrene spheres

An advantage of polystyrene (PS) or other polymer templates over silica is that the organic nature of polymer facilitates clean and thorough cleansing of templates by simple calcinations or hot organic solvent dissolution, while its susceptibility to high temperature also makes it ineligible for fabrication route that required heat treatment. Similar to silica templates, polystyrene was commonly used as templates in form of spheres, which were discrete when dispersed in aqueous media and unsuitable for the formation of monolithic and uniformly continuous framework [75-77]. In order to construct 3D structure with such templates, two strategies have been employed: 1) transforming PS colloids into 3D colloidal crystal before templating, [78] similar to silica colloids; 2) self-assembly of such templates with other materials (e.g. graphene) to induce extra porosity. [79]

As for methods aiming to achieve 3D colloidal assembly, fabrication of PS colloidal crystal, in this aspect, is close to that of silica particles, except for the organic nature of polymer that enables the fastening of PS into a periodically arranged pattern at a much lower temperature around 100°C. So far, diverse methods have been developed to transfer PS onto conductive substrate, which might broaden the application of PS spheres in assembling 3D electrodes[68]. Those methods mainly include: 1) dropping PS colloids onto lateral substrate surface along with follow-up evaporation; [80] 2) deposition onto vertically suspended substrate in PS colloids by evaporation of solvent along the surface; [81-83] 3) a dip-wetting method by drawing substrates out of PS colloids at a constant speed and angle; [84-87] 4) electrophoretic deposition of PS spheres onto conductive substrate. [88] However, 3D colloidal crystals formation is normally time-consuming and requires extra labor when compared to procedures that directly integrate PS spheres into macroporous matrices. As an example exploiting self-assembly of templates with graphene, Choi *et al.* [89] developed 3D macroporous graphene frameworks (embossed chemically modified graphene, denoted as e-CMG) for SCs by filtration technique (as shown in Fig. 10a). Two suspensions, PS and graphene oxide suspensions, were mixed at pH 2 that maintain their uniformity in the media without sedimentation. Afterwards, the mixture was filtered and meanwhile adjusted to pH 6 to promote the electrostatic interaction between PS and graphene oxide, directed by the opposite charge carried at such pH. The resultant self-supported graphene framework collected after removal of PS possessed high mass of 10 mg for a single electrode and delivered a specific capacitance calculated to be 202 F/g at 1 A/g (Fig. 10c), which was two times higher than that of the film prepared without PS (93 F/g). An all-3D asymmetric supercapacitor device was also fabricated as shown in Fig. 10b with e-GMC as a negative electrode and a positive electrode obtained by depositing MnO_2 onto e-GMC, demonstrating an energy density of 44 Wh kg^{-1} and a power density of 25 kW kg^{-1} within a potential window of 2.0V.

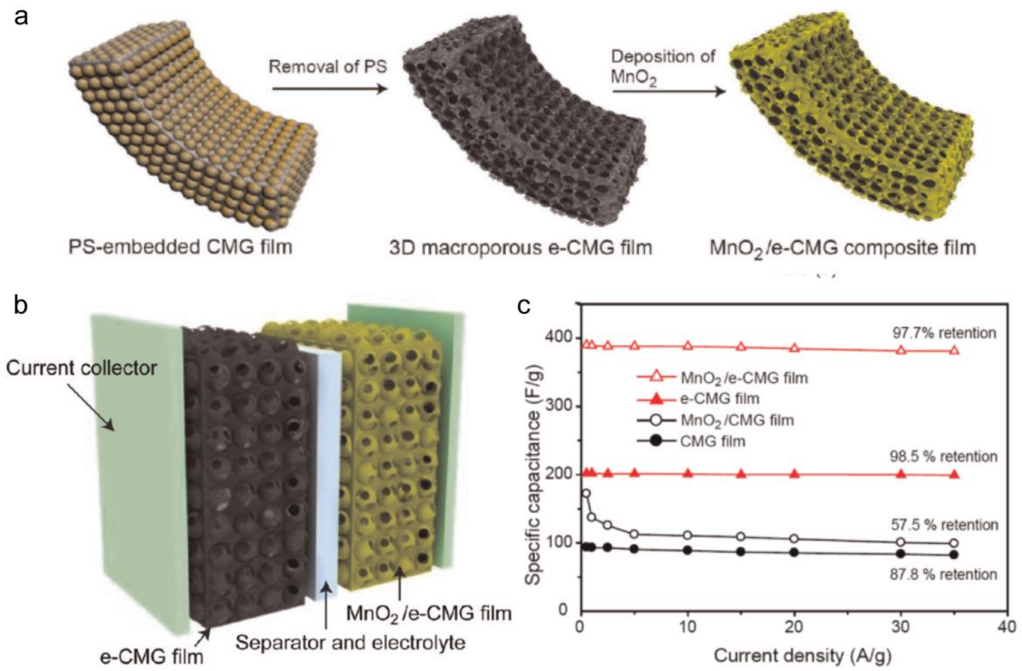

Fig. 10. (a) Schematic illustration of the assembly process of e-CMG and MnO2/e-CMG composites film. (b) Rate performance shown in specific capacitance of various electrodes against current density. (c) Image giving an illustration of the all-3D device assembling. Reproduced from Ref. [89] with permission from American Chemical Society.

3.4 Metal organic frameworks (MOFs)

Metal organic frameworks are of great interests as an intriguing template for 3D supercapacitor electrode materials since its unique structure that can be designed through bottom-up route and that is the very feature which distinguishes it from common hard templates. [90-92] Most of aforementioned templates used to achieve 3D scaffold are considered from a top-down perspective. For example, NFs can cast out graphene foams that inherit the original frameworks, an upper-level structure to give out lower-level one. On the contrary, the structure of MOF itself is assembled from microscopic molecular with certain geometric symmetry and sites to coordinate with metal ions, leaving a much larger flexibility for 3D structure designing. Undoubtedly, it is known that some types of MOFs possess excellent activity for electrochemical capacitor from multiple previous researches and those will not be considered in this section since they cannot be classified as templating methods. [93-95] However, converting the MOF frameworks into highly porous carbon frameworks that are active for SCs application is a templating method to build up 3D structure, as presented by Fig. 11a, a carbonization example of MOFs to produce sheet-like porous carbon (Fig. 11b). [96] From this perspective, MOFs should be referred to as sacrificial and chemical templates in some cases since the exploiting of such templates involves a chemical conversion process. [20] Up to date, researches pertaining to such sacrificial templating methods had explored the electrochemical properties and tentatively examined the applications of those MOF derived carbons in SC devices. For the first time, Liu *et al.* carbonized a MOF-5 framework impregnated with polymerized furfuryl alcohol (FA), resulting a structure of which the N_2 sorption isotherms indicated the existence of different pore sizes spanning from micro- to macro-pores (Fig. 11c). A specific capacitance of 159 F/g at a scan rate of 50 mV/s was observed, as shown by CV diagram in Fig. 11d. [96] Since then, porous carbon deriving from MOFs was further studied by researchers. [97-103] Despite the high surface area achieved by MOFs templates, those 3D nanoporous carbons have relatively low specific capacitance (no more than 350 F/g), which is probably due to the low theoretical capacitance of carbon itself. The abnormal phenomena were also attributed to the low conductivity in some of those works, in which it was concluded that low carbonization temperature brought about larger porosity but lesser conductivity. [99] To the best of our knowledge, such high surface area might have a great impact on its electrochemical properties once the hindrance of their low conductivity was resolved, and further improvements still need to be done for MOFs templating method. More interestingly, a continuous metal organic gel was deployed as self-templated carbon source through a three-step gel-aerogel-carbonization method by Wei *et al.*, fabricating a monolithic carbon electrode. [104] However, the electrode was merely examined for lithium sulfur batteries and its electrochemical performance in SCs is unknown. Thus, monolithic 3D electrode derived from metal organic gel, in this respect, might still be of interest and research value.

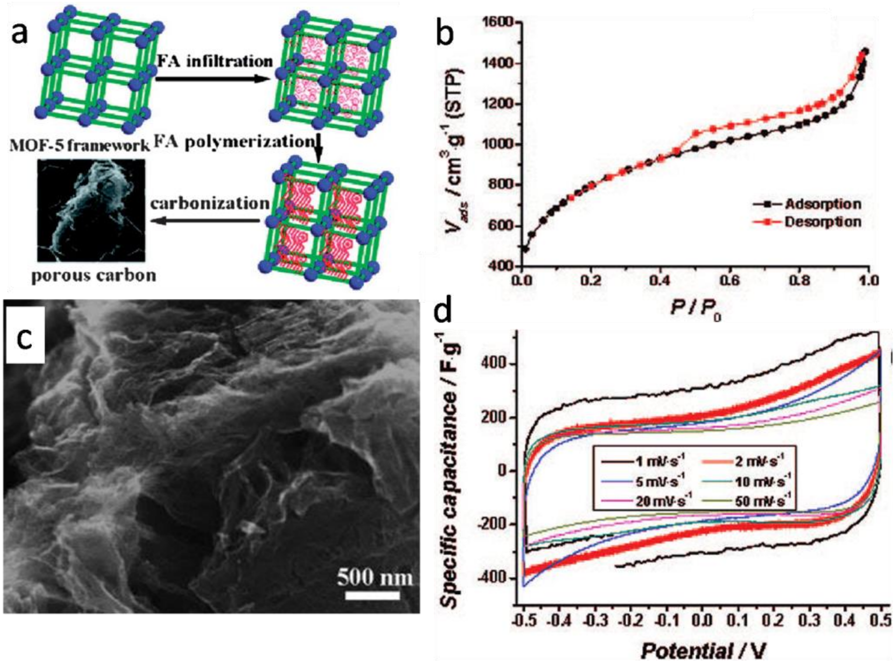

Fig. 11. (a) Schematic illustration of carbonization procedure of MOF-5 infiltrated with FA precursors. (b) the N_2 sorption isotherms for NPC electrode. (c) SEM image of the sheet-like carbon. (d) Cyclic voltammetry of NPC in 1 M H_2SO_4 at different scan speeds. Reproduced from Ref. [96] with permission from American Chemical Society.

3.5 Other templates

Driven by increasing demand for flexible and wearable devices, various templates other than NF, silica and polystyrene have been employed to construct 3D electrodes. However, synthesis procedures were quiet similar even though numerous templates have been used for 3D electrode. Thereby, this part will only give a brief description of templates materials applied as scaffolds for 3DSC electrode. Among those templates mostly were backbones with macroscopic skeletons[105-109] and particle templates[22, 110] coupled with self-assembly graphene

For instance, Liu *et al.* improvised a polypyrrole stabilized cable-type 3D electrode with deposited MnO_2 middle layer and graphene inner layer as electron conducting pathway, delivering a maximal areal capacitance of 0.52 F/cm^2 at a scan rate of 1 mV/s that maintained almost constant at scan rate up to 100 mV s^{-1}. [107]Other examples with macroscopic backbone include a 3D hybrid electrode of nanoporous gold/nanocrystalline MnO_2 (reported by Lang *et al.*, giving a capacitance of 1145 F/g[105]) and a template method employing carbonized cotton cloth developed by Pang *et al.*. [108] Except for those, particle templates (e.g. $CaCO_3$) were also exploited in assisting self-assembly of graphene or as molds for hollow structure design, similar to silica and polystyrene templates. Meng *et al.* [110] developed a facile assembly method using $CaCO_3$ formed in situ in the GO dispersion process to produce a free-standing porous graphene film (3D-RGO). The in-situ-formed $CaCO_3$ intercalated in between the graphene stacks and afterwards porosity was increased by removal of $CaCO_3$ with HCl solution. This work demonstrated a flexible 3D-RGO/PANI electrode with specific capacitance of 362 F/g at 1 A/g indicating capacitance retention of 94%.

So far, numerous endeavors have shown the shifting mosaic of template methods because properties of templates vary according to the intrinsic nature of materials. However, unresolved problems, especially for the controversial application of such procedure in large scale manufacturing, still need to be explored and solved out..

4. None-template fabrication of 3D electrodes

Although great progresses have been made in template-assisted fabrication of 3D electrodes, to some extent, the existence of template might have a negative effect on their capacitive behavior, such as their chemical stability during the charge-discharge process. Moreover, the use of template will obviously increase the total weight of the electrode, resulting in an inevitable damage of specific power and energy densities. Attempts have been made to remove the templates, which always require complicate steps, harsh conditions, high cost and long time consuming. In this regard, quantities of alternative reliable synthetic routes without templates have been developed. These methods mainly rely on the self-assembly of low-dimensional monomers, multistep assembly of hierarchical structures and post-treatment of 3D natural precursors. In this section, we will provide a review of non-template synthesis method of 3D electrodes for different types of materials, along with their properties and SCs application.

4.1 Carbon material

As a large family, carbon materials are perceived as the most common SC materials attributed to their fascinating properties including abundant sources, low cost, superior conductivity, ultralong stability and environmental friendliness.[8, 14] Among various carbon materials, most efforts of researchers have focused on the design of graphene based 3D electrodes due to their unique lamellar structures and hollow tubular structures respectively. Additionally, composite electrodes constructed by carbon materials with other pseudocapacitive materials become immediate areas of research focus, which always possess hierarchical structures. Dual functions are utilized for carbon materials, contribution of the high capacitance and excellent conductive pathway for the electron transport.

4.1.1 Graphene

Since Novoselov *et al.* first discovered graphene by micromechanical exfoliation of bulk graphite in 2004[111], the study on graphene achieved explosive development. Graphene is a kind of one-atom-thick 2D single layer of sp2-bonded carbon, allowing a high electron mobility, strong mechanical strength and high accessible high surface area (2600 m^2/g).[112] These unique properties enable graphene very promising as monomer to assemble 3D architecture. In previous sections, we have introduced some strategies for fabricating 3D graphene architecture with the assistance of templates like nickel foam, polystyrene spheres. In this part, we mainly focused on those 3D graphene electrodes synthesized through none-template methods.

In 1985, Hummers *et al* [113] reported chemically exfoliated graphite oxide (GO) through oxidation of natural graphite powder with strong oxidants. Inspired by this method, wet chemical approaches were rapidly generalized to construct 3D graphene structures through the gelation of GO dispersion followed by reduction to reduced graphite oxide (RGO). Crumbled graphene can be directly obtained from the GO dispersion through a directly drying method or an aerosol spray drying method.[114-118] In these conditions, graphene sheets tend to form highly crumpled surface and high pore volume, which can prevent them from agglomerating and re-stacking in a certain term. Such characteristics could enable significant improvement in terms of various performance parameters of SCs. For instance, Ruoff's group[118] firstly fabricated crumpled ball-like GO particles using aerosol spray drying method. (Fig. 12a) During this process, the GO suspension was transformed into the fine droplets, and the GO sheets formed crumpled and hollow shapes accompanying the evaporation. Then, the obtained GO particles were reduced and expanded by treating in a microwave oven. Finally the crumpled graphene ball was activated through thermal treatment with KOH. Consequently, the unique three-dimensional pore structures in the produced crumbled graphene offer rise to a remarkable BET surface area value of up to 3290 m^2/g. When tested as SC electrodes in a two-cell symmetrical cell with an ionic liquid electrolyte, the device displayed rectangular shapes for CV curves and almost unchanged capacitance values with scan rate change from 100 to 400 mV/s. (Fig. 12b) Electrochemical impedance spectroscopy was performed to further evaluate the electrochemical behavior of the crumbled graphene based device as shown in Fig. 12c and 12d. A nearly ideal capacitive behavior was suggested by the vertical slope observed for Nyquist plot at the low-frequency region. The resistance calculated by extrapolating the vertical portion of the plot to the real axis was only 3.75 Ω, indicating the low ESR value of the crumbled graphene based device. Simultaneously, the crumbled graphene based device exhibited phase angles of close to -90^o at low frequency regions, which further confirmed the pure capacitive behavior.(Fig. 12d) The relaxation time τ_0 calculated at the phase angle of -45^o is only 1.67s, corresponding to its superior rate capability.

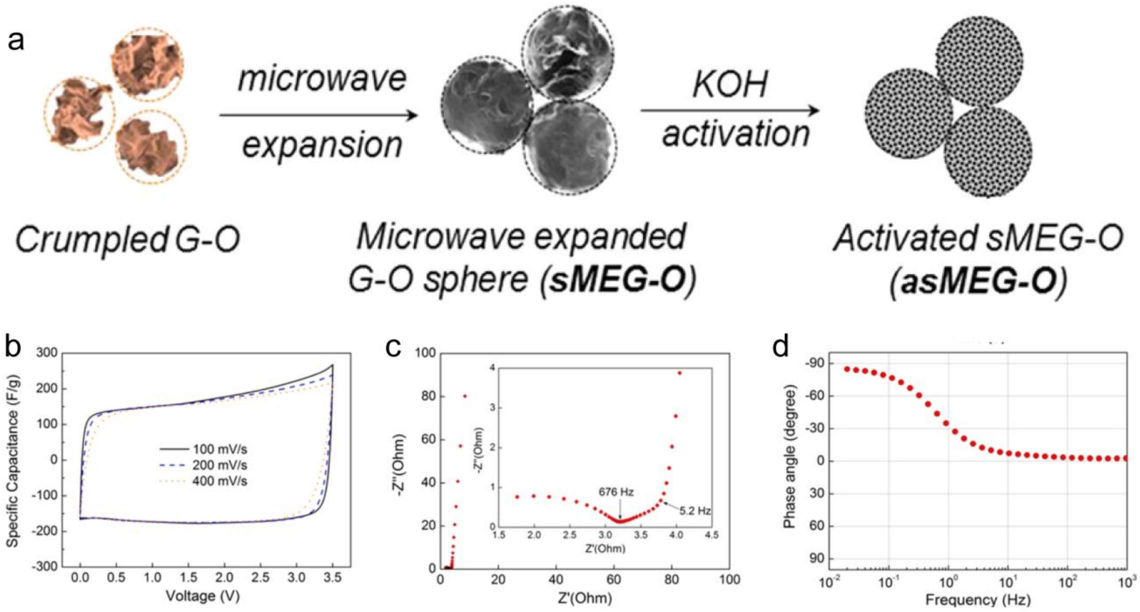

Fig. 12. (a) Schematic of the fabrication of highly porous crumbled graphene with hierarchical pore structures. (b) Cyclic voltammetry curves for different scan rates obtained for this crumbled graphene. (c) Nyquist plot showing the imaginary part versus the real part of impedance. Inset magnifies the data in the high-frequency range. (D) Impedance phase angle versus frequency. Reproduced from Ref. [118] with permission from American Chemical Society.

The stabilization of GO sheets in water is believed by a force balance between the inter-planar van der Waals attractions among GO sheets and the electrostatic repulsions from edge-bound hydrophilic oxygenated groups. The self-assembly of GO sheets would occur if the balance is broken and one of efficient methods is hydrothermal method. For example, Shi and his coworkers [119] reported the self-assembled graphene hydrogel through a direct hydrothermal reaction. As shown in Fig. 13a, the as-prepared graphene hydrogel is mechanically strong, showing no deformation with high weight loading. Moreover, a well-defined and cross-linked 3D porous structure was observed from the SEM image (Fig. 13b). Such high specific surface area grants the hydrogel a large electric double layer capacitance with 175 F/g at a scan rate of 10 mV/s in aqueous electrolyte. Additionally, chemical doping with foreign atoms was believed to be an efficient way to improve the electronic characteristic of graphene materials, which could enrich free charge-carrier density and improve the electrical conductivity of graphene materials. Besides, pseudo-capacitance was always introduced into graphene by substituting carbon atom in the graphene plane for foreign atoms. Adding additives into reaction media of hydrothermal reaction is a convenient strategy for the fabrication of foreign atom doped 3D graphene architectures. Recently, one or more kinds of foreign atoms are tried to be doped into graphene through this method, like nitrogen[120, 121], sulphur,[83, 122] phosphorus[123, 124] and boron[120, 125]. Wu *et al.* [120]have realized the co-dope of nitrogen and boron into graphene by adding ammonia boron trifluoride (NH_3BF_3). The interconnected frameworks with macroporous architectures were well maintained, which are favorable for ion diffusion and electron transport in bulk electrode. An all-solid-state symmetric SC device was also fabricated based on this graphene, exhibiting a large energy density of 8.65 Wh/kg. Additionally, efforts have been tried to assemble hydrogel composites of graphene and pseudocapacitive materials as reported by Xie *et al.*[126], combining 3D graphene hydrogel with porous MnO_2. This unique structure featured the hydrogels with a combination of high conductivity and high specific capacitance.

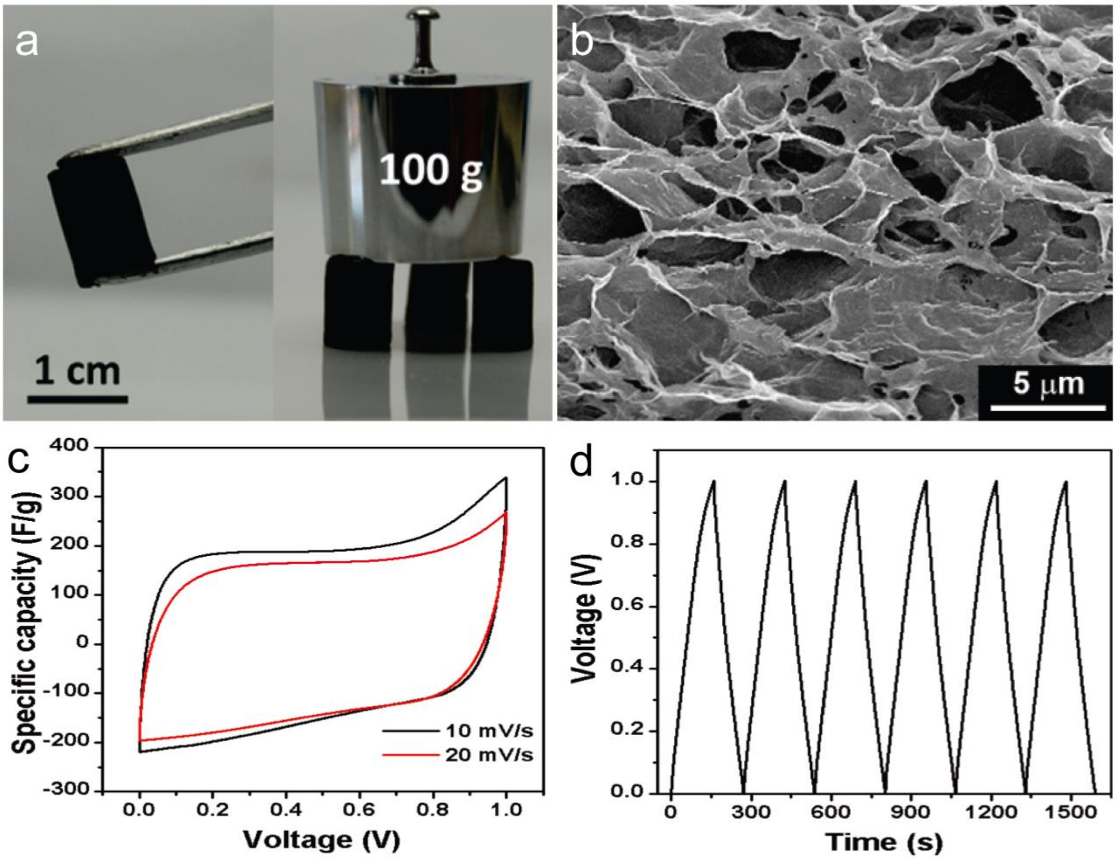

Fig. 13. (a) Photographs of a strong RGO aerogel allowing easy handling and supporting weight. (b) SEM image of RGO aerogel interior microstructures. (c) Cyclic voltammograms (CV) of RGO aerogel based SC at two different scan rates. (d) Galvanostatic charge/discharge curves of RGO aerogel based SC at a constant current of 1 A/g. Reproduced from Ref. [119] with permission from American Chemical Society.

Filtration through a porous membrane filter is another common method to construct 3D graphene architecture from GO dispersion. In this situation, the graphene macroscopically appear as thin paper. Ruffo and his co-workers creatively assembled free-standing graphene oxide (GO) paper for the first time through directly filtration of dispersed GO aqueous solution.[127] Immediately following, Li *et al.* [128-130] applied this technique to fabricate graphene paper by a further reduction step and investigated its SC application. The individual graphene sheet was arranged in a nearly parallel manner through the directional flow, yielding a freestanding structure with density of ~1.8 g/cm^3. A symmetric SC device with organic electrolyte based on wet graphene paper was further assembled, reaching a large voltage window of 4 V. The SCs could offer a large specific capacitance of 273.1 F/g, power density of 776.8 kW/kg and energy density of 150 Wh/kg.[129] Moreover, they further exchange the water in wet graphene paper with a mixture containing volatile and non-volatile liquid (H_2O/H_2SO_4), as shown in Fig. 14. [130] After the volatile part in graphene was completely evaporated, porous dry graphene film was obtained (Fig. 14a). The packing density of this film could be easily tuned from 0.13 g/cm^3 to 1.49 g/cm^3 through changing the ratio of volatile and non-volatile liquid (Fig. 14b, 11c and 14d). Particularly, a high gravimetric capacitance of 203.2 F/g was reached for the graphene film with packing density of 0.13 g/cm^3, while a high volumetric capacitance of 255.5 F/cm^3 was exhibited for the graphene film with packing density of 1.33 g/cm^3 at 0.1 A/g in aqueous electrolyte.

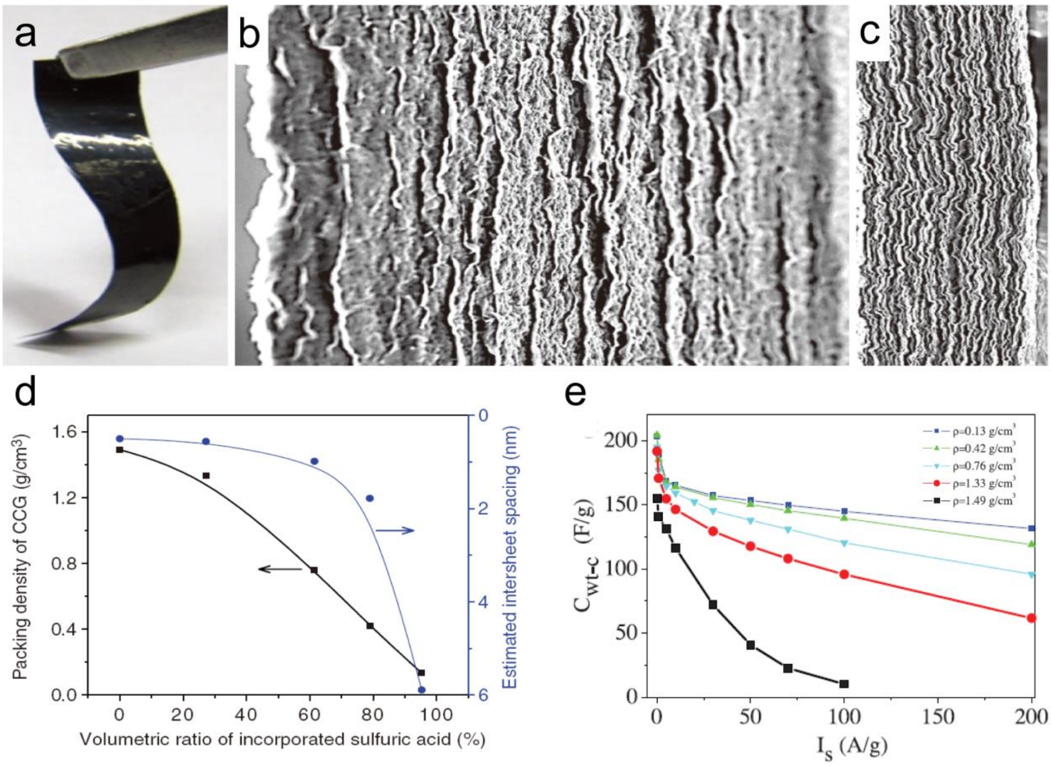

Fig. 14. (a) A photograph showing the flexibility of the film. SEM images of cross sections of the obtained graphene films containing (b) 78.9 volume percent (vol. %) and (c) 27.2 vol. % of H_2SO_4, respectively, corresponding to $\rho = 0.42$ g/cm^3 and $\rho = 1.33$ g/cm^3. (d) The relation between the volumetric ratio of incorporated electrolyte and the packing density as well as the estimated inter-sheet spacing. (e) Gravimetric capacitances with varied charging/discharging current densities. Electrochemical characterization of graphene films in 1.0 M H_2SO_4 (ρ = 0.13, 0.42, 0.76, and 1.33 g/cm^3, respectively). Reproduced from Ref.[130] with permission from the American Association for the Advancement of Science.

However, a critical issue encountered in this process is the easy aggregation or restacking of graphene sheets into graphitic structure due to the π-π stacking interaction and van der Waals attraction among their basal planes. The restacking severely hampers the diffusion of ions into the interspace among the densely packed graphene sheets resulting in large loss of energy storage capability. In view of this problem, insertion of spacer between graphene sheets is applied to prevent the restacking of them. Many studies have been focused on these composites graphene film using different kinds of spacer materials like CNTs,[131-133] metal oxides,[126, 134-138] polymers,[110, 139] and the others[140]. For example, Fan *et al.* [131]have added $Co(NO_3)_2$ into the graphene suspension as catalyst, followed by CNTs grown in-between graphene layers through a CVD reaction (Fig. 15a). As shown in Fig. 15b and 15c, a typical graphene-CNT-graphene sandwich structure has been obtained, which possessed a layered structure with CNT spaces without impeding its electrical conductivity (40.7 and 180.1 S/m in vertical and parallel directions, respectively). The unique structure combines the high-rate transportation of electrolyte ions and electrons, comprehensive utilization of double-layer capacitance for carbon materials and high pseudo-capacitive behavior of residual cobalt, exhibiting an excellent capacitance of 385 F/g at 10 mV/s.

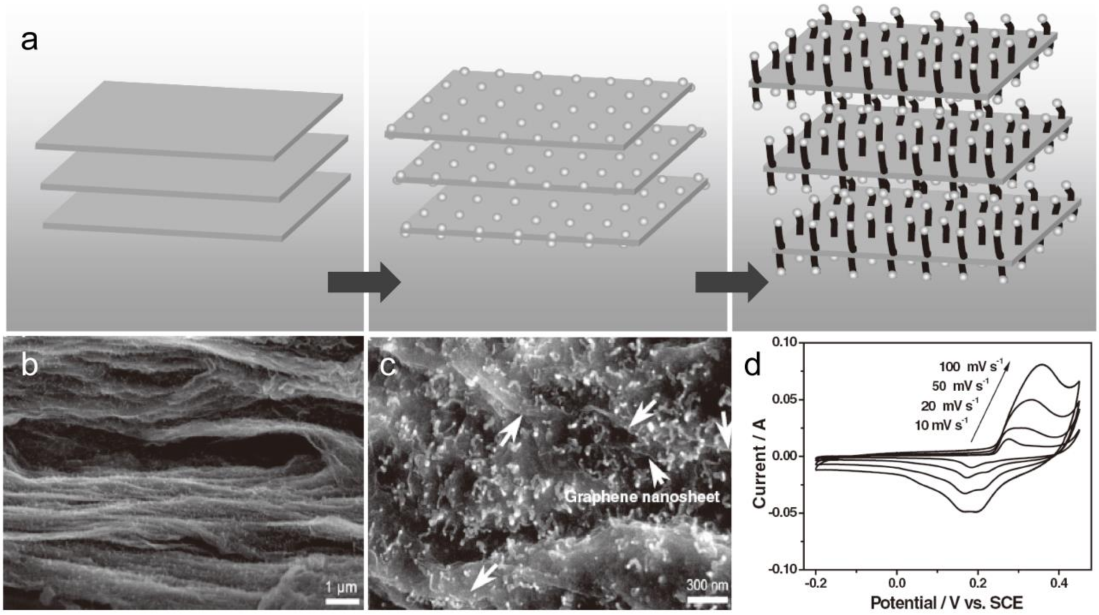

Fig. 15. (a) Illustration of the formation of CNT/graphene sandwich (CGS) structures. (b-c) SEM images of CGS (d) Electrochemical performances of CGS: CV results measured at scan

rates of 10, 20, 50, and 100 mV/s. Reproduced from Ref. [131] with permission from WILEY-VCH Verlag GmbH & Co. KGaA, Weinheim.

Other novel methods were applied to fabricate 3D graphene architectures for SC application. [141-144] For instance, Kaner with his group [143] took advantage of light scribe technique to exfoliate graphene sheets. Chen *et al.* [144] reported a leavening strategy to form porous structure in compact graphene structures. The obtained graphene foams with open pores and continuous cross links was used to assemble flexible symmetric SCs, showing a high specific capacitance of 110 F/g. Maiti *et al.*[142] used electrostatic attraction to realize the self-assembly of 3D graphene film. A Zn foil was put into the graphene oxide suspension, the electrons were transferred from the Zn foil to graphene oxide sheets due to the low reduction potential of Zn. Meanwhile the graphene oxide was reduced to graphene and assembled into 3D structures with water as spacer, giving a RGO foam with density of 0.44 mg/cm^2 and high electrical conductivity of 103.3 S/m. The SC based on this kind of 3D graphene film delivered a remarkable energy density of 2.73 μWh/cm^2. Most recently, our group[141] directly applied the modified Hummers method to graphite paper, and macroscopically fabricated a kind of 3D graphene scaffold (Fig. 16). After a combine process of Hummers method and freezing technique, the volume was substantially expanded more than 10 times (Fig. 16a, 16b and 16c). The high quality of graphene sheet was confirmed from SEM and TEM images (Fig. 16d and 16e). This unique 3D structure not only exhibited a superior capacitive properties (the largest specific capacitance of 331.3 F/g at 10 mV/s), but also worked well as scaffold to support other electrochemical active materials. As an example, PANI nanorods were deposited on its surface, and the specific capacitance of as-prepared composite electrode based on the whole mass (18 mg/cm^3) reached 931.8 F/g at 10 mV/s.

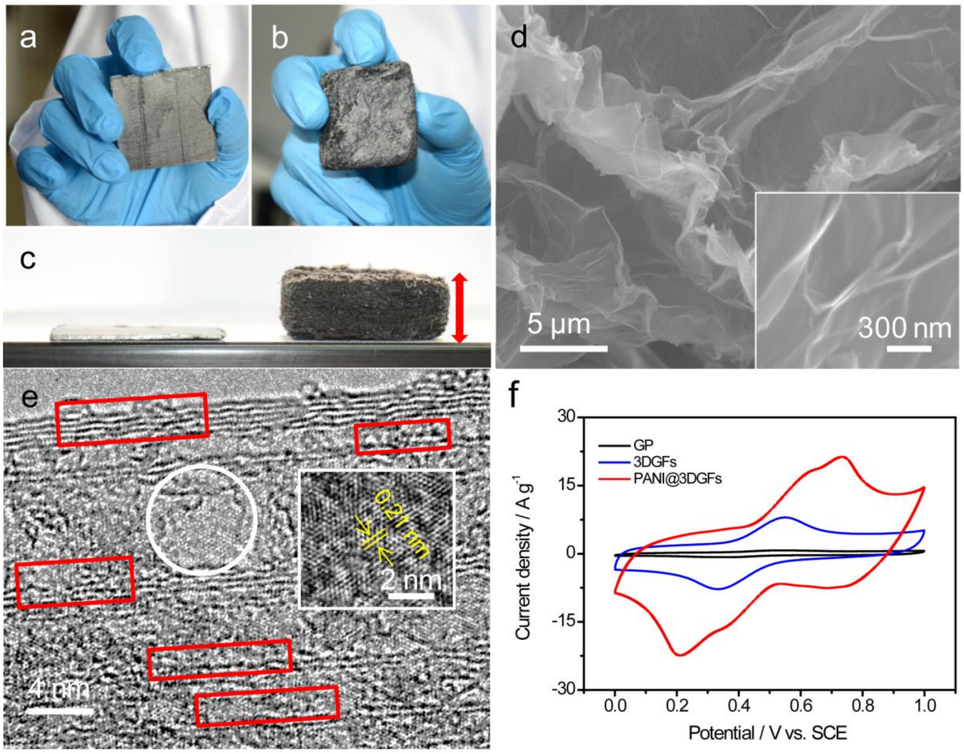

Fig. 16. Photographs of (a) graphite paper (GP), (b) 3D graphene foams (3DGFs), and (c) their comparison. (d) SEM and (e) TEM images of 3DGFs. (f) CV curves collected at 20 mV/s of GP, 3DGFs and PANI@3DGFs electrodes. Reproduced from Ref.[141] with permission from WILEY-VCH Verlag GmbH & Co. KGaA, Weinheim**.**

4.1.2 Other carbon materials

Besides graphene, other kinds of carbon materials were also tried to be applied into fabricating 3D SC electrodes. Among them, the electrochemical performance of CNTs has been widely evaluated since their discovery by Iijima in 1991[145], considering their unique tubular porous structures, extremely high electrical conductivities and outstanding mechanical properties. There are mainly two strategies to fabricated 3D CNTs based electrode. One is using the CNTs as "wires" to weave into a 3D architecture. For example, Kohlmeyer *et al.*[146] fabricated a kind of CNTs organ-gels using Fc-PPE and Fc-PPETE as chemical cross-linkers. After heat treatment, the as-prepared CNTs aerogels are mechanically stable and stiff, showing highly porous of 99%, excellent electrical conductivity of 1-2 S/cm and large specific surface area of 590–680 m^2/g. However, rare investigation was conducted on the capacitive behavior of pure CNTs based 3D electrodes. That may be due to their low specific capacitance relying on the double layer capacitance. In view of this, main attention has been put onto the combination of CNTs with pseudo-capacitive materials. Several attempts have tried to synthesize textile-like 3D CNTs based electrodes.[121, 147-149] In particular, Lu with his group[121, 147, 148] have developed a series of tangled 3D architecture of CNTs with V_2O_5 nanowires. Most recently, they have evaluated the energy storage ability of this CNTs/V_2O_5 3D composite as sodium-ion SC electrode. As shown in Fig. 17a and 17b, V_2O_5 nanowires and CNTs interpenetrate into 3D networks with interconnected pore channels, which enable fast access of the electrolyte, effective electron transport, shortened ion diffusion paths. In addition, the typical layered structure of V_2O_5 with an interplanar spacing of 0.95 nm for (001) plane allowed a fast sodium ion intercalation and deintercalation process during the pseudocapacitive charge storage process occurs. Firstly, 1 M $NaClO_4$ in propylene carbonate (PC) was utilized as electrolyte, while sodium foil was selected as both the counter and reference electrodes. Fig. 17c shows a main capacitive contribution of 82% to the charge storage process, in which lies a much larger ratio for pseudo-capacitance than double-layer-based capacitance. Then they assembled coin-type asymmetric SCs using CNTs/V_2O_5 as cathode and commercial activated carbon as anode. These novel sodium-ion

SCs exhibited a largest energy density of 38 Wh kg^{-1} at a high mass loading of 3 mg/cm^{2}, even higher than those of previously reported lithium-ion SCs. The other strategy is directly depositing active materials on the surface of CNTs, which can efficiently take use of a synergistic effect. Zhang *et al.* have respectively coated manganese oxide and PANI on the CNTs using electrochemical deposition method, achieving 3D architecture with hierarchical pores.[126] The MnO_2/CNTs composite with a mass loading of 0.037 mg/cm^{2} achieved a very high specific capacitance of 199 F g^{-1} (corresponding volumetric capacitance 305 F cm^{-3}), a high rate capability of 50.8% at 77 A g^{-1}, and a long-term electrochemical stability of 20000 cycles. On the other hand, the PANI/CNTs 3D composite also achieved a high specific capacitance of 1030 F g^{-1} and an enough cyclic stability of 5000 cycles. Recently, vanadium nitride (VN) nanoparticles were synthesized on the CNTs through reactive RF magnetron sputtering method by Zhang *et al* (Fig. 18a).[150] As shown in Fig. 18b, monocrystalline VN particles were uniformly coated on the surface of CNTs. A remarkable specific capacitance of 289 F g^{-1} was demonstrated for these 3D nanostructures in 1 M KOH electrolyte at 20 mV s^{-1}. (Fig. 18c and 18d) Furthermore, more than 80% capacitance retention was reached even at a very high scan rate of 1 V s^{-1}, indicating their remarkable rate capability.

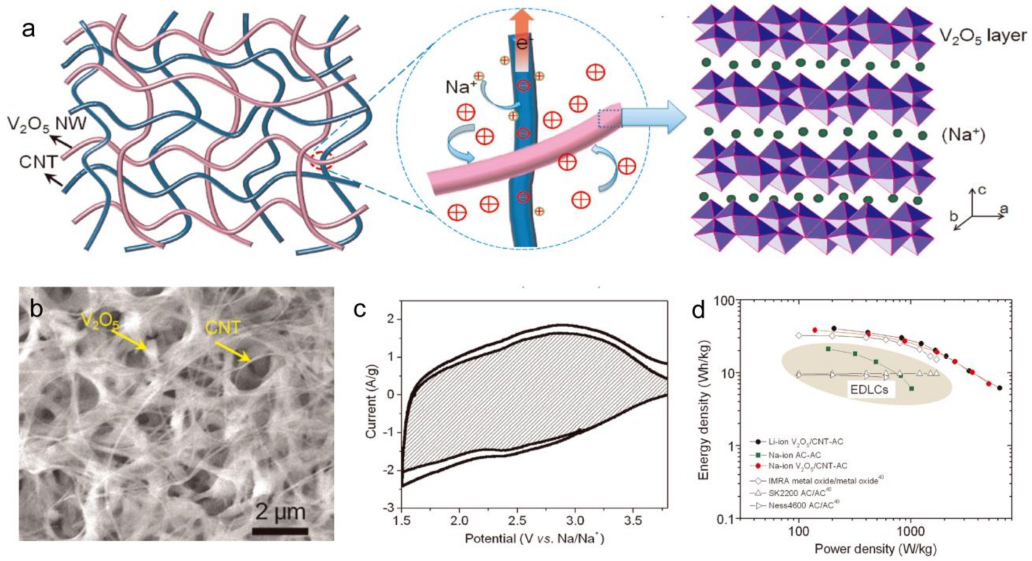

Fig. 17. (a) Schematic of a nanocomposite consisting of interpenetrating networks of V_2O_5 nanowires and CNTs, intimate contacts between the V_2O_5 nanowire and CNTs facilitating charge transport, and Na^+ intercalation within the V_2O_5 layer structure. (b) SEM image of a V_2O_5/CNT nanocomposite demonstrating nanowire V_2O_5 networks penetrated with CNTs. (c) Capacitive and diffusion-controlled contribution to charge storage. The capacitive current is shaded and compared with the total measured current. (d) Ragone plots of Na-ion and Li-ion asymmetric SCs made from a V_2O_5/CNT nanocomposite anode and an activated carbon cathode. Reproduced from Ref. [147] with permission from American Chemical Society.

As a derivative of CNTs, carbon nanohorns are also perceived as crooked and twisted graphene sheets with irregular horn-like shapes, which are easily self-assembled into 3D structured Dahlia-like spheres with diameters below 100 nm.[151-156] Unlike CNTs, the advantage of carbon nanohorns lies not only in large specific surface area but also easy permeation of the electrolyte. To address their closed wall structure, Yang *et al.*[153] realized the hole-opening of carbon nanohorns through a very easy oxidation treatment. Through the nanowindows formed from the holes in the wall of carbon nanohorns, solvated ions in electrolyte are accessible to the internal spaces, hence resulting in a substantially enriched electronic double layer capacitance. The carbon nanohorns with hole-opening structure achieved a much higher specific capacitance of 116 F/g at discharge current density of 1 mA/cm^2, compared to only 66 F/g for the pure carbon nanohorns. Composite 3D electrodes based on carbon nanohorns were also tried by the researcher with the aim of engineering a well defined, ordered pore structure and introducing pseudocapacitance.[151, 152, 156] For example, Hata with his group[156] has reported a novel 3D CNTs/carbon nanohorns composite film with well-defined pore structures. Attributed to the superior ability to hold sufficient electrolytes within its void volume, facile ion transport was obtained, leading to a maximum power rating of 990 kW/kg.

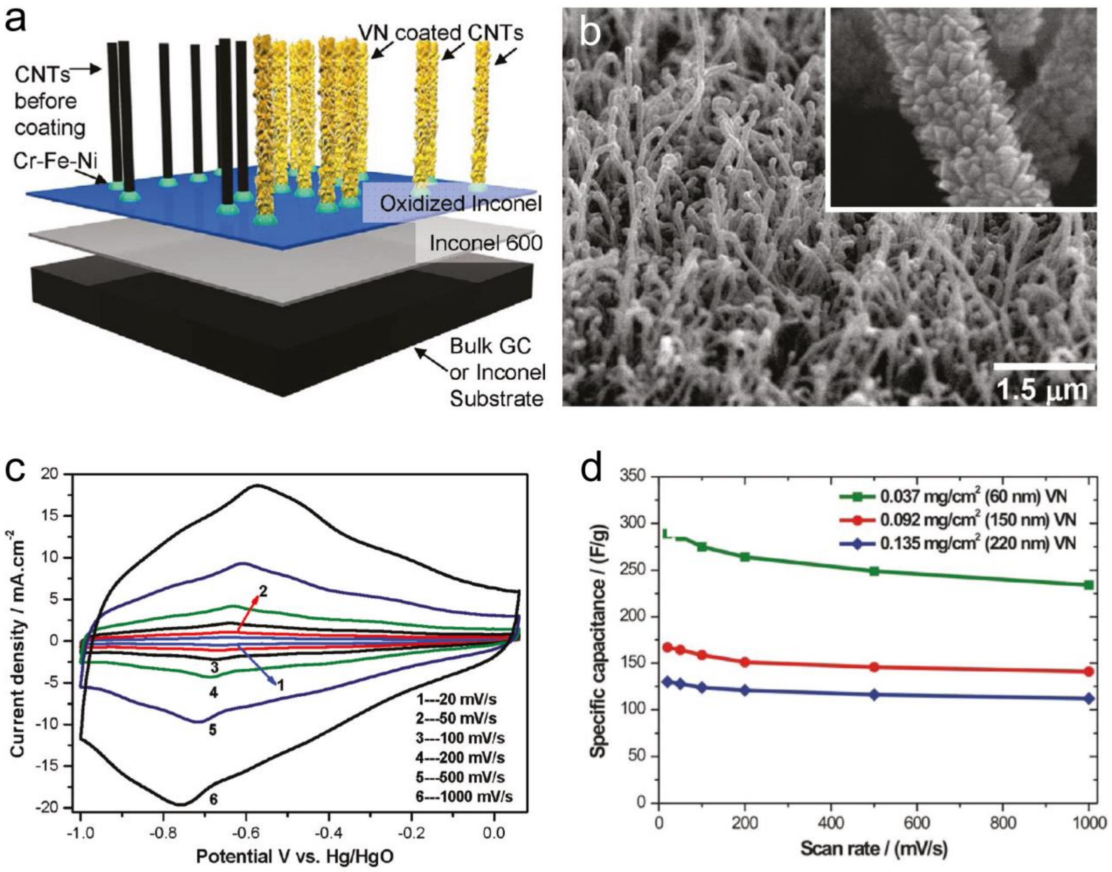

Fig. 18 (a) A schematic summarizing the synthesis process and ultimate morphology of the VN/CNT 3D array. (b) Increasing magnification SEM micrographs of VN/CNT. (c) CV curves of VN/CNT in the potential range of 1.0 to 0.06 V, at different scan rates from 20 to 1000 mV/s. (d) Relationship between the specific capacitance versus scan rate. Reproduced from Ref. [150] with permission from American Chemical Society.

Several attentions have also been paid to the construction of 3D electrodes based on hierarchical carbon materials with high surface areas and rich pore structures.[157-160] Hierarchical pores including micro-, meso- and macro- pores were constructed in this structure. Among them, micro-pores are perceived as the main contribution to energy storage, meso- and macro-pores can accelerate the kinetic process of the ion diffusion in the electrode corresponding to the improvement of power density. In this term, these 3D hierarchical pore structures could guarantee a superior electrochemical performance. Cheng with his group[159] has synthesized a 3D periodic hierarchical porous graphitic carbon (HPGC) using phenolic resin as carbon source. The texture of the macroporous cores with diameters of about 1 mm was clearly revealed from Fig. 19a, which severs as good ion-buffering reservoir. The TEM image in Fig. 19b shows meso-pores with diameters between 10 to 50 nm uniformly distribute within the thin walls. Furthermore, considerable micro-pores were observed through the pore-size distribution derived using nonlocal density functional theory (Fig. 19c). Such abundant hierarchical pores enable the HPGC as a very promising SCs material with high specific capacitance and fast charge-discharge ability. Even at a fast discharge rate of only 3.6s, the HPGC also can deliver an especially outstanding energy and power density of 22.9 Wh/kg and 23 kW/kg. (Fig. 19d) Carbon aerogels (CA) are also a superior candidate for highly conductive porous matrix, which own a 3D well-connected through-pore structure.[161-167] These hierarchical carbon aerogels are always obtained from pyrolysis of polymer materials. As an example, Gutierrez *et al.*[168] recently reported 3D carbon aerogels with hierarchical pores from PPO-PEO-PPO block copolymer. Short chain block copolymer was selected as surfactant to create carbon aerogel monoliths, which possesses a bimodal porosity in micro and macro range. The resulting carbon aerogel achieved a remarkable electronic conductivity of 2.5 S/m, meanwhile, a maximum electronic double layer capacitance of 225 F/g. Furthermore, hierarchically porous graphite particles were designed by Chen *et al.* based on an aerosol process, using sucrose as carbon source. [148] Through rational design of production process, this method enable continuous, scalable synthesis of such carbon species, which contain hierarchical pore structure and graphitized shell. Symmetric SC based on these graphite particles achieved a gravimetric energy density of 30 Wh/kg at a power density of 270 W/kg, which is considerably higher than those of active carbon and CNT based symmetric SCs, even based on the high mass loading of this work (4-12 mg). Moreover, researchers also paid attention to the fabrication of 3D carbon aerogel based composite electrodes with pseudocapacitive materials like MnO_2[162, 166], $NiCo_2O_4$[165], SnO_2[163], polypyrrole[164], *etc.* Lu with his group[165, 166] successively combined phenolic resin derived carbon aerogel with MnO_2 and $NiCo_2O_4$. The specific capacitances reached 503 and 1700 F/g for carbon aerogel/MnO_2, and carbon aerogel/ $NiCo_2O_4$ electrodes at 25 mV/s, respectively.

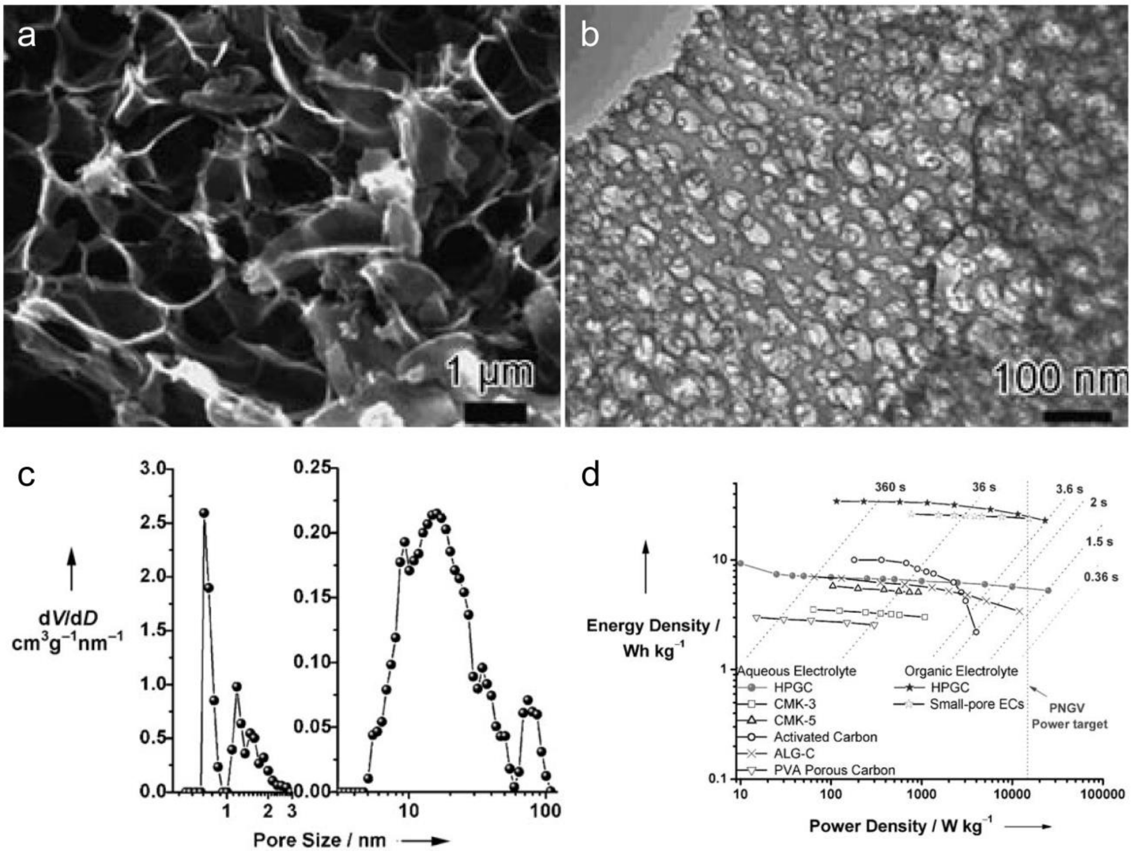

Fig. 19. (a) SEM image of the macroporous cores of the HPGC material. (b) TEM image of the mesoporous walls and micro-pores. (c) Pore-size distribution of the HPGC material. (d) CV results measured at sweep rates of 20, 50, 100, and 200 mV/s in an alkaline electrolyte (6 mol/L KOH). Reproduced from Ref. [159] with permission from WILEY-VCH Verlag GmbH & Co. KGaA, Weinheim

Carbide-derived carbon with natural properties inherited from its initial soft organic was also a key source for the fabrication of 3D architecture. To date, various kinds of natural carbides were explored like dead leave[169], banana peel[170], silk proteins[171], rice husk[172], stover[173], corn cob[174], waste paper[175, 176], and *et. al*. For instance, Ogale's group [169] developed a single-step pyrolysis method to treat dead leaves. Internal activation was suggested to be provided by the natural constituents in the leaves. Different capacitive behaviors were confirmed by treating different kinds of dead leaves (Neem and Ashoka leaves), which is attributed to different constitution and composition of the bio-source. The obtained 3D porous carbon derived from Neem leaves achieved an ultrahigh surface area of about 1230 m^2/g, an remarkable specific capacitance of 400 F/g, and an high energy density of 55 Wh/kg at 0.5 A/g in 1 M H_2SO_4. Most recently, Corn cob shell was reported to be applied to synthesize 3D carbon based architecture by Genovese *et al.*[174] Fig. 20a depicts their synthesis strategy, containing remove of the amorphous surroundings, pyrolysis, exfoliation process with thermal-chemical flash. As expected, the obtained 3D biochar appears as agglomeration of thin carbon sheets, similar to dry graphene. (Fig. 20b) The thin sheet-like carbon structure shown in Fig. 20c clearly revealed the exfoliated carbon sheets. Due to its high surface area, superior porosity and introduced oxygen functionality, the exfoliated biochar demonstrated a high specific capacitance of 221 F/g, 78% capacitance retention at a fast discharge current of 40 A/g and stable electrochemical performance within 5000 cycles. Hierarchical porous carbon foams were also prepared from banana peel through a self-assembly strategy by Lv *et al.*[170] With the abundant natural porous structure formed from the biopolymers in cell walls, banana peel absorbed large amount of zinc ions and phenolic compounds as a metal-organic framework style. After a carbonization process, the hierarchical porous carbon foams were obtained containing macroporous cores, mesoporous and microporous channels, which possessed a high specific surface area of 1650 m^2/g. As expected, a remarkable specific capacitance of 206 F/g was reached at a current density of 1 A/g. In addition, it is reported that up to over 4 kg of waste paper was generated for per household each week. Recycling or reuse of waste paper as energy storage material is one of the promising solution for its disposal. Simple KOH activation of waste paper was reported for SC application by Kalpana *et al.*[175] Significantly, a much lower charge-transfer resistance was observed for carbon derived from waste paper than carbon aerogel from RF gel as illustrated from the EIS results. Meanwhile, a more close to vertical line in the low frequency region for carbon derived from waste paper further confirmed its pure capacitive behavior. A maximum specific capacitance of 180 F/g was revealed from the CV results at a 2 mV/s. Table 1 summarizes the mass loading of active materials, conductivity and capacitive performance of the 3D carbon electrodes prepared through template-assisted and template-free methods.

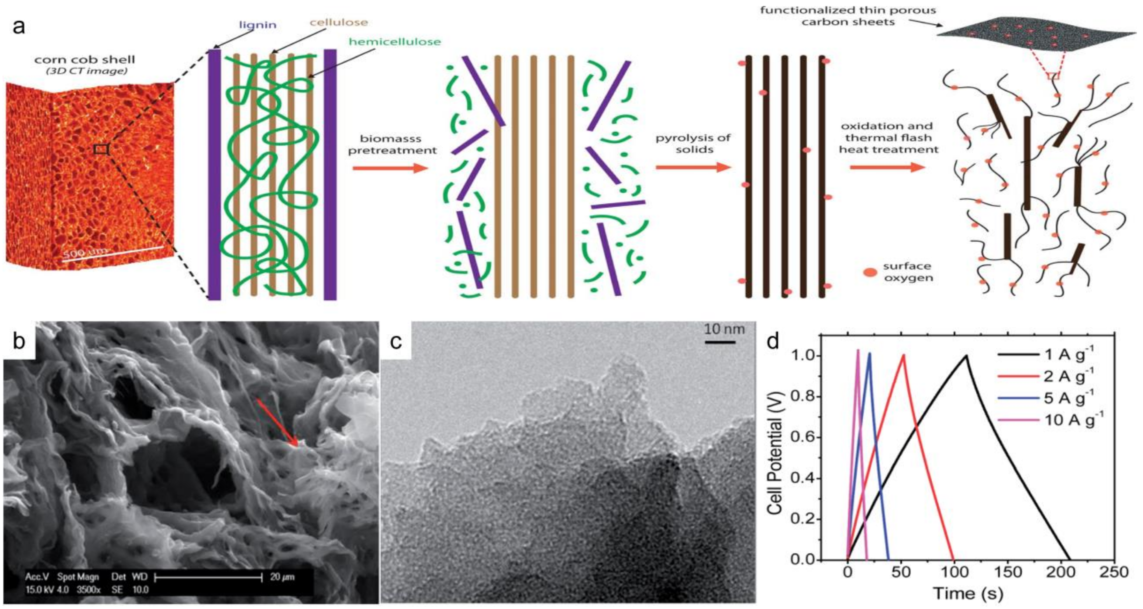

Fig. 20. (a) Schematic representation of the synthesis strategy for the exfoliated corn cob biochar. (b) SEM images of the exfoliated biochar. (c) TEM image of the exfoliated biochar depicting a layered structure of thin microporous nanosheets. (d) Galvanostatic charge/discharge of exfoliated biochar electrodes in a symmetric 2 electrode SC cell with 0.5 M H_2SO_4 electrolyte at rates from 1 to 10 A/g. Reproduced from Ref. [174].

Table 1. Summarized properties of 3D carbon electrodes and their corresponding capacitive performances

Electrode description	Fabrication method	Mass loading	Conductivity	Specific capacitance	Cycling performance	Ref.
The first graphene foam derived from NFs	Nickel foam templating	~ 5 mg/cm^3	10 S/cm	-	-	24
ERGO foam	Nickel foam templating	-	-	156.9 F/g at 1 A/g	-	33
CNT-ERGO	Nickel foam templating	-	-	280.4 F/g at 1 A/g	-	33
GA-MC	Silica templating	-	-	~226 F/g at 1 mV/s	No capacitance loss after 5000 cycles at 2 A/g	74

GMCS–NH_3	Silica templating	5.0-7.0 mg/cm^2	381 S/m	29.6 F/g at 0.1 A/g	94% retention after 1000 cycles at 0.5 A/g	177
3D hierarchical porous carbon	Silica templating	~5.5 mg/cm^2	-	118.1 F/g	-	72
e-CMG	PS templating	10 mg for a whole electrode	1204 S/m	202 F/g at 1 A/g	-	89
3D-RGO/PANI film	Other templates ($CaCO_3$)	0.25 mg/cm^2 ,	-	362 F/g at 1 A/g	90% retention over 5000 cycles at 5 A/g	110
NPC carbon	Other templates (MOFs)	-	-	159 F/g at 50 mV/s	-	96
NPC800	Other templates (MOFs)	-	-	190 F/g at 3 A/g	98% retention rate after 1500 cycles at 3 A/g	103
Self-assembled graphene	Non-template method	-	Up to 4.9	175 F/g at 10	-	119

hydrogel			mS/cm	mV/s		
Nitrogen and boron co-doped GAs c	Non-template method	-	-	26.2 F/g at 100 mV/s	100% capacitance retention after 1000 cycles at 2 A/g	120
GO paper from filtration	Non-template method	1.8 g/cm^3	-	-	-	127
Self-stacked, solvated graphene	Non-template method	0.45 mg/cm^2	-	273.1 F/g	-	129
Electrolyte-mediated CCG	Non-template method	Tunable from 0.13 g/cm^3 to 1.49 g/cm^3	-	~200 F/g at 0.1 A/g	-	130
Carbon nanotube/graphene sandwich	Non-template method	-s	40.7 and 180.1 S/m in vertical and parallel directions	385 F/g	Increased with 20% after 2000 cycles at 200 mV/s	131

Laser scribed graphene	Non-template method	-	1738 S/m	265 F/g at 250 A/g	>97% of its initial response after 10,000 cycles	143
rGO foams	Non-template method	-	-	110 F/g	-	144
Interfacially gelated rGO foam	Non-template method	0.44 mg/cm^2	103.3 S/m	33.8 mF/cm^2 at 1 mA/cm^2	97.8% retention after 4000 cycles at 10 mA/cm^2	142
PANI@3DGF	Non-template method	18 mg/cm^3	252.0 S/cm for 3DGF	931.8 F/g at 10 mV/s	70.2% retention after 1000 cycles at 40 mV/s	141
CA1-800 monolith	Non-template method	-	2.5 S/cm	120-130 F/g at 150 mA/cm^2	95% retention after 10000 cycles at 100 mA/cm2	168
Hierarchically porous graphite particles	Non-template method	4-12 mg/cm^2	-	102 F/g at 1 A/g	98% retention rate after 5000 cycles at 2 A/g	178

Dead leaf derived carbon	Non-template method	-	0.588 S/cm (1.7 Ω/cm)	250-400 F/g at 0.5 A/g	-	169
Carbon-based microporous nanoplates	Non-template method	-	$\sim 1.15 \times 10^4$ S/m	Over 100 F/g at 70 A/g	>93% retention over 10000 cycles at 2.5 A/g	171
Exfoliated biochar nanosheets from corn cob	Non-template method	1.5 mg/cm^2	-	221 F/g at 0.5 A/g	97% retention over 5000 cycles at 0.5 A/g	174

4.2 Metal oxides

Metal oxides are indispensable pseudocapacitive materials for the SC electrodes, such like MnO_2,[73, 179] NiO, [180] [181] Co_3O_4,[182-184] VO_x,[185, 186] Fe_2O_3[187] *et al.* Generally, metal oxides can allow higher specific capacitance than carbon materials, which further enhance the energy density of the SCs.[188] It is because that these metal oxides can not only store energy through electronic double layer capacitance, but also through the reversible faradic reaction between them and ions in electrolyte. However, the main drawback severally limiting their generalization of SC application is their unsatisfied conductivity. [188] Aiming at this point, rationally designed 3D structure can ensure an efficient channel for the electron transportation. The construction methods of 3D metal oxides electrodes can be briefly divided into one-step self-assembly and multistep assembly. In this section, the main strategies for the construction of 3D metal oxides architectures are summarized. Notably, we introduced the 3D metal oxides/carbon materials in the front section of this paper, hence we will not repeat it in this section.

4.2.1 One step self-assembly of 3D metal oxide electrodes

The designed self-assembly of 3D metal oxides theoretically base on the crystal growth law. All kinds of synthesis methods were applied to the synthesis of metal oxides crystals by researchers, like electrochemical deposition, hydrothermal method and solvent thermal method *et al*. [126, 180, 189-196] Controllable fabrications of 3D architectures were realized through tuning different synthesis parameters during the growth process of metal oxide crystal.

Among them, hydrothermal method is a easily adjustable method for the synthesis of nanocrystalline metal oxides by the optimization of reaction time, precursor, temperature, additive and so on. Chen *et al.*[194] used hydrothermal method to fabricate MnO_2 nanostructures with well-controlled morphology and crystal phase as shown in Fig. 21. As the reaction time increasing, the morphology of MnO_2 transferred from 3D nanoflower to tangled nanowires, then to dispersive nanotube, at the same time, the crystal phase converted from δ-MnO_2 to α-MnO_2. Vajtai and his co-workers[189] synthesized the macroscopically production of thin V_2O_5 thin nanosheets with a thickness of only 4 nm through a hydrothermal method. By using these nanosheets as building blocks, self-assembly of 3D architectures were constructed after a further freeze-drying method. The 3D architecture was made up of thin walls and multilevel pores, providing easy access of electrolyte to V_2O_5 surface (Fig. 22a and 22b). As the energy storage application, the 3D V_2O_5 electrode reached a large specific capacitance of 451 F/g in Na_2SO_4 aqueous electrolyte (Fig. 22c), and the energy density achieved 107 Wh/kg at a high power density of 9.4 kW/kg (Fig. 22d).

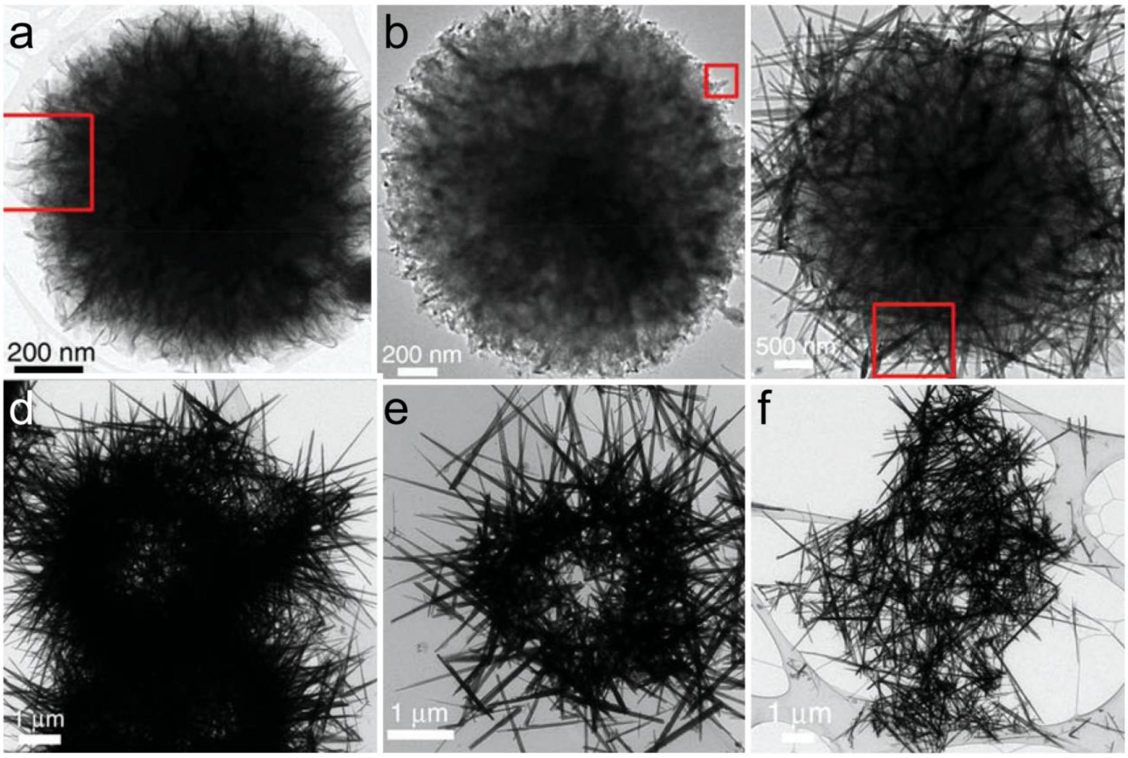

Fig. 21. TEM images of the MnO_2 nanostructures obtained at different hydrothermal reaction times. (a) MnO_2-1 h; (b) 1.5 h; (c) 2 h; (d) 4 h; (e) 8 h; (f) 12 h. Reproduced from Ref. [194] with permission from WILEY-VCH Verlag GmbH & Co. KGaA, Weinheim.

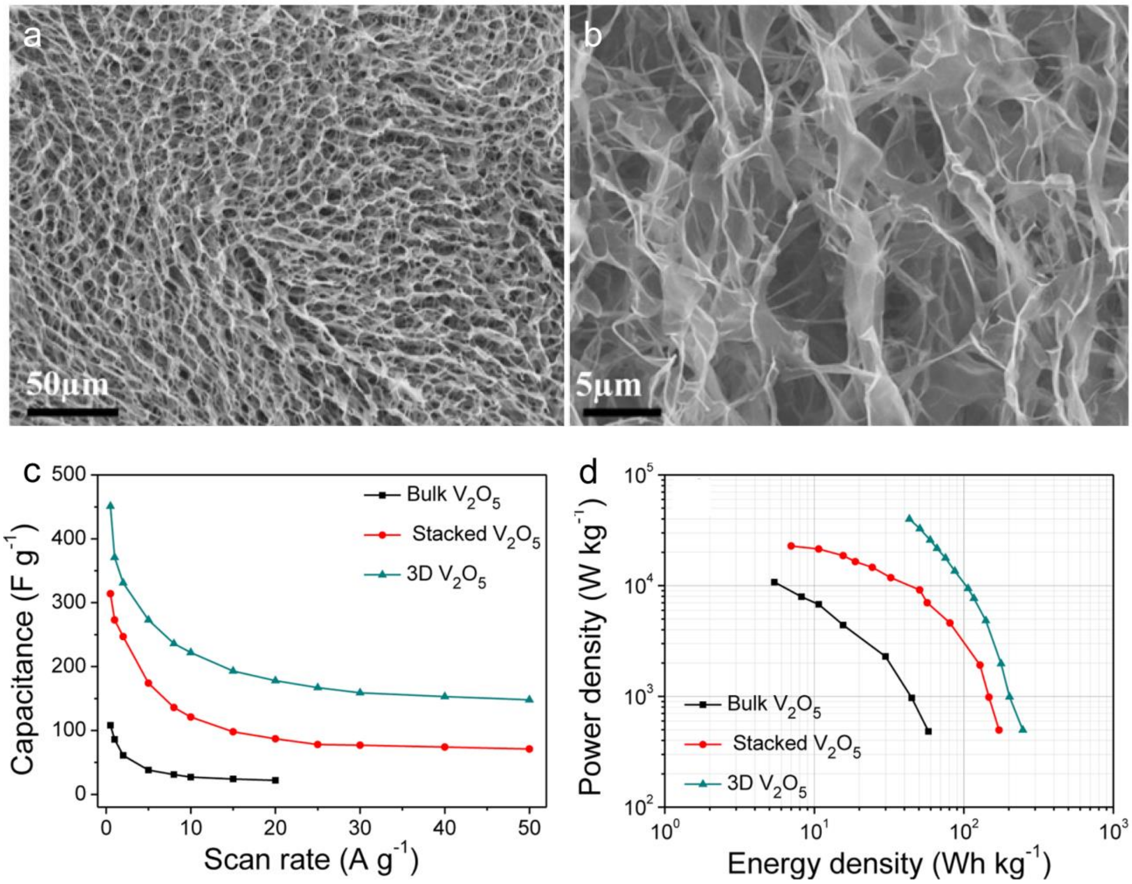

Fig. 22. (a-b) Typical field emission scanning electron microscopy (FESEM) images of the 3D V_2O_5 architecture constructed from nanosheets. (c) Specific capacitances calculated from galvanostatic charge/discharge with various current densities. (d) Power density and energy density of V_2O_5 3D architecture, stacked V_2O_5 film, and bulk V_2O_5 electrodes. Reproduced from Ref. [189] with permission from American Chemical Society.

Electrochemical deposition method was also adopted to fabrication metal oxide materials with 3D morphology. Such like Huang *et al.* [190]deposited 3D vanadium oxide (VO_x) on the graphite substrate with a $VOSO_4$ based electroplating electrolyte, maximum specific capacitance of which reached 180 F/g. 3D nanoporous NiO film prepared by an electrochemical route[180] achieved a high surface area of 264 m^2/g. On this occasions, 3D architectures were generally assembled by low-dimensional nanostructures like VO_x nanowires[190] and NiO nanosheets[180].

4.2.2 Multistep assembly of 3D metal oxide composite electrodes

Some investigations were also conducted to assemble 3D metal oxide composite electrode step by step. Generally, backbone material with low dimension is firstly fabricated, followed by deposition of branch materials. One dimensional ZnO material is chose as favorable backbone material due to its mature synthesis method. For example, two-step seed-assisted hydrothermal process was used to construct 3D ZnO nanoforest as shown in Fig. 23a.[197] The deposition of a thin MnO_2 shell was followed, maintaining the 3D nanoforest morphology (Fig. 23b and 23c). For comparison, 1D ZnO@MnO_2nanowires were also fabricated. Fig. 23d depicts the galvanostatic charge/discharge curves of the ZnO@MnO_2 nanowires and nanoforest at a same discharge current density. As a consequence, the substantially longer discharge time for ZnO@MnO_2 nanoforest indicated its much higher areal capacitance than ZnO@MnO_2 nanowires (Fig. 23d). The calculated areal capacitance reached 31.3 mF/cm^2, which is almost 5 times that of the corresponding nanowires electrode (Fig. 23e). Similarly, MnO_2 and NiO nanoflakes were synthesized step by step on ZnO nanowires,[181, 198] which also exhibited a superior capacitive behavior as SC electrodes.

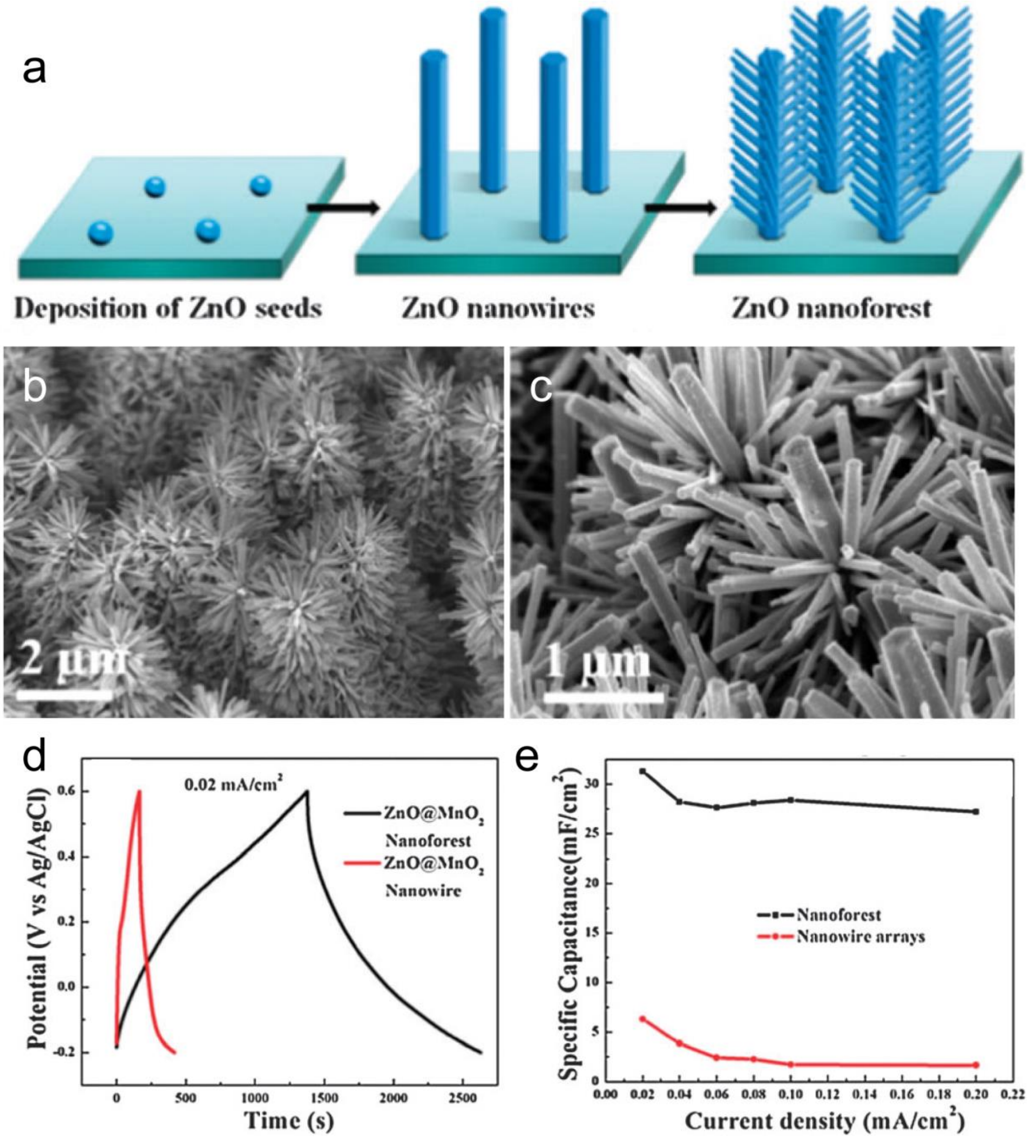

Fig. 23. (a) Schematic illustration of the fabrication process for the designed 3D ZnO nanoforest counterpart. (b-c) Typical SEM images of the synthesized 3D ZnO@MnO_2 core-shell forest of nanotrees. (d) Galvanostatic charge/discharge curves of the 3D ZnO@MnO_2 core-shell nanoforest and nanowire arrays at a current density of 0.02 mA/cm^2. (e) Specific discharging capacitances at different current densities of electrodes made of nanoforest and nanowire arrays. Reproduced from Ref. [197].

Moreover, more 3D metal oxide-metal oxide composite structures were designed and fabricated by researchers such like Co_3O_4@NiO,[181] Co_3O_4@MnO_2,[199] SnO_2@V_2O_5,[200] Co_3O_4@NiOH,[37] Co_3O_4@Fe_2O_3[201], CuO@MnO_2[202] and $MnMoO_4$@$CoMoO_4$[203] backbone-branch structures. Taking advantage of the synergistical effect from both capacitive backbones and branches, these 3D structures usually delivered favorable electrochemical performance. Particularly, great achievements were made by Fan with his group.[37, 181, 198, 199] For instance, Co_3O_4 nanowires through hydrothermal method were firstly fabricated on FTO substrate, then NiO nanoflakes were uniformly coated on the Co_3O_4 cores by a further chemical bath strategy. [181] (Fig. 24a and 24b) On one hand, the well-separated NiO nanoflakes distributed on the Co_3O_4 nanowire cores enable the full exposure of both active material to the ions in electrolyte. On the other hand, good mechanical stability and electronical conductivity was guaranteed by the synergistical effect of cores and shells. Therefore, the composite electrode achieved a much higher capacitance than single Co_3O_4 nanowire and NiO nanoflakes. (Fig. 24c). Moreover, the Co_3O_4@NiO electrode also exhibit a good excellent stability with a specific capacitance of 853 F/g maintained at 2 A/g after 6000 cycles. However, it is worth noting that such 3D structures based on the metal oxides can only fasten the electronic transport along the electrode in a certain term, but not improve their natural poor conductivity. Table 2 summarizes the mass loading of active materials, conductivity and capacitive performance of the 3D metal oxides based electrodes prepared through template-assisted and template-free methods.

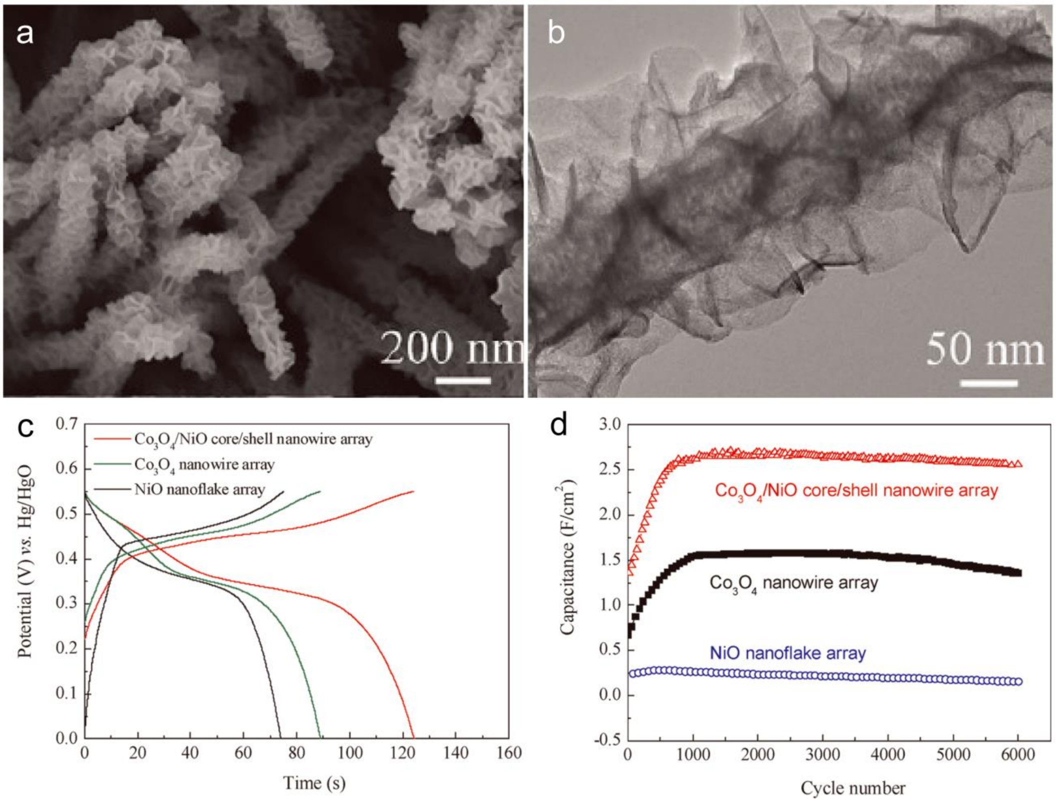

Fig. 24. (a) SEM and (b) TEM of Co_3O_4@NiO core/shell nanowire arrays grown on FTO substrate. (c) Charge/discharge curves at the 10th cycle and (d) cycling performances at 2 A/g. Reproduced from Ref. [181] with permission from American Chemical Society.

Table 2. Summarized properties of 3D metal-oxide based electrodes and their corresponding capacitive performances

Electrode description	Fabrication method	Mass loadings	Conductivity	Specific capacitance	Cycling performance	Ref.
3D graphene/Co_3O_4 nanowire composite	Nickel foam templating	-	-	~1100 F/g at 10 A/g	~1100 F/g after 500 cycles	25
MnO_2-coated freestanding 3D graphene foam	Nickel foam templating	0.85-9.8 mg/cm^2	55 S/cm	1.42 F/cm^2 at 2 mV/s	82% retention at 1.5 mA/cm^2 after 5000 cycles	26
3D graphene/CNFs/MnO_2 composite	Nickel foam templating	0.1 mg/cm^2	55 S/cm	946 F/g at 2 mV/s	94.1% retention after 1000 cycles at 10 A/cm^2	28
$CoMoO_4$ NHC-like films-3D graphene foam composite	Nickel foam templating	0.51 mg/cm^2	-	2741 F/g at 1.43 A/g	96.36% retention at 400 A/g after 100000 cycles	29
MnO_2 /3DGH	Nickel foam	1.5 mg/cm^2	-	345 F/g at 10	-	32

	templating			mV/s		
MnO_2-ERGO	Nickel foam templating	-	-	422.5 F/g at 1 A/g	-	33
MnO_2-ERGO//CNT-ERGO device	Nickel foam templating	-	-	69.4 F/g at 0.5 A/g	84.4% retention after 10000 cycles at 5 A/g	33
Nickel foam	-	-	350 S/cm	-	-	24
ZnO@Co3O4	Nickel foam support	2.0 mg/cm^2	-	857.7 F/g at 1 A /g	78% retention at 6 A/g after 6000 cycles	35
CN@NCH	Nickel foam support	2.0 mg/cm^2	-	2550 F/g at 1 A/g	92.70% retention after 5000 cycles at 20 A/ g	36
CoO@NiOOH	Nickel foam support	~3.0 mg/cm^2	-	798.3 F/g at 1.67 A/g	96.7% retention after 2000 cycles at 10 A/g	37
$Ni(OH)_2$ nanosheets on	Nickel foam support	1.8-2.0	-	2384.3 F/g at 1	75% retention after 3000	39

nickel foam		mg/cm^2		A/g	cycles at 5 A/g	
Activated nickel foam	Nickel foam support	25.5 mg/cm^2 including nickel foam	-	2.0 F/cm^2 at 8 mA/cm^2	Increased from 0.47 to 1.27 F/cm^2 after 100000 cycles at 100 mV/s	23
3D CoO@Ppy nanowire array electrode	Nickel foam support	~ 2.0 mg/cm^2	-	2223 F/g at 1 mA/cm^2	~ 99.8% capacitance after 2000 cycles at 20 mA/cm^2	44
Cobalt Oxide Nanobrush-Graphene@$Ni_xCo_{2x}(OH)_{6x}$	Nickel foam support	~2.0 mg/cm^2	-	2550 F/g at 1 A/g	92.70% retention after 5000 cycles at 20 A/g	36
Ultrathin Mesoporous $NiCo_2O_4$ Nanosheets	Nickel foam support	0.4 mg/cm^2	-	1450 F/g at 20 A/g	94% retention after 2400 cycles	49
Networked $NiCo_2O_4$/MnO_2 BNH arrays	Nickel foam support	~1 mg/cm^2	-	1891 F/g at 100 mA/cm^2	98.4% retention after 3000 cycles	50

GA-RuO_2	Silica templating	-	-	~348 F/g at 100 mV/s	-	74
MnO_2/e-CMG	PS templating	10 mg for a whole electrode	-	389 F/g at 1 A/g	-	89
e-CMG//MnO2/e-CMG device	PS templating	10 mg for a whole electrode	-	-	95% retention after 1000 cycles at 1 A/g	89
PPy-MnO_2-CNT-cotton thread	Other templates (cotton thread)	Up to 3 mg/cm^2 for SWCNT coating	-	0.52 F/cm^2 at 1 mV/s	96% after 3000 cycles at 3.33 mA/cm^2	107
Nanoporous gold/nanocrystalline MnO_2	Other templates (noble metal)	-	-	1,145 F/g at 50 mV/s	85% retention up to 1000 cycles	105
V_2O_5/CNT nanocomposite	Non-template method	3 mg/cm^2	-	~400 C/g at 2	~80% retention after 900	147

				mV/s	cycles at 60 C	
VN/CNT 3D array	Non-template method	0.037 mg/cm^2 for VN	~23 S/cm (43.5 mΩ/cm)	289 F/g at 20 mV/s	-	150
3D V_2O_5 architecture	Non-template method	-	-	521 F/g at 5 mV/s	~90% retention after 4000 cycles 5 A/g	189
Nanostructured MnO_2	Non-template method	2~3 mg/cm^2	-	110 F/g at 1 A/g	Capacitance increased after 5000 cycles	194
3D porous vanadium oxide	Non-template method	-	-	150-160 F/g at 250 mV/s	-	190
3D nanoporous NiO	Non-template method	-	-	1776 F/g at 1 mV/s	97.9% over 1000 cycles	180
ZnO@MnO_2 nanoforest	Non-template method	-	-	31.30 mF/cm^2 0.02 mA/cm^2	-	197

MnO_2–NiO nanoflakes	Non-template method	-	-	0.101 F/cm^2	96.4% retention after 1500 cycles at 8.5 mA/cm^2	198
ZnO/NiO Core/Shell Nanowire Arrays	Non-template method	3 mg/cm^2	-	853 F/g at 2 A/g	95.1% after 6000 cycles at 2 A/g	181
Co_3O_4 nanowire @ MnO_2 nanosheets	Non-template method	1.5 mg/cm^2	-	480 F/g at 2.67A/g	97% after 5000 cycles at 11.25 mA/cm^2	199
CuO@AuPd@MnO_2 NWs	Non-template method	0.55 mg/cm^2	-	493 F/g	100 % over 5000 cycles at 100 mV/s	202
Hierarchical $MnMoO_4$/$CoMoO_4$ nanowires	Non-template method	-	-	187.1 F/g at 1A/g	98% after 1000 cycles at 3A/g	203

4.3 Other materials

Conducting polymers, including polyaniline (PANI),[204-206] polypyrrole (Ppy),[207] poly(3,4-ethylenedioxythiophene) poly(styrene sulfonate) (PEDOT-PSS)[208, 209] *et al.* are also believed to be a kind of promising SC electrode materials, due to their low cost, environmentally friendly property, high conductivity under doped state, high electronic storage capacity, and adjustable redox activity through chemical modification. 3D porous structures were easily fabricated through self-assembly of low dimensional nanostructures.[204-209] Common preparation methods mainly divide into electrochemical polymerization[204-207] and directly chemical polymerization[208, 209]. For example, Yu *et al.*[204] constructed a porous 3D network consisting of numerous PANI nanofibers on a stretchable CNTs based substrate by a one-step electrochemical deposition method with a solution of 0.1 M aniline and 1 M H_2SO_4 (Fig. 25). The obtained PANI based electrode exhibited a remarkable specific capacitance of 1023 F/g, and corresponding areal capacitance of 481 mF/cm^2. Such stretchable electrodes also provide great chance for the fabrication of high-performance stretchable SC devices. As a demo, a solid-state stretchable symmetric SC was assembled (denoted as PANI-SSC), which use H_2SO_4/PVA as electrolyte as shown in Fig. 25c. The as-fabricated PANI-SSC device not only achieved an excellent energy density of 0.15 mWh/cm^3, but also displayed stable capacitive properties even under both static and dynamic stretching conditions. (Fig. 25d)

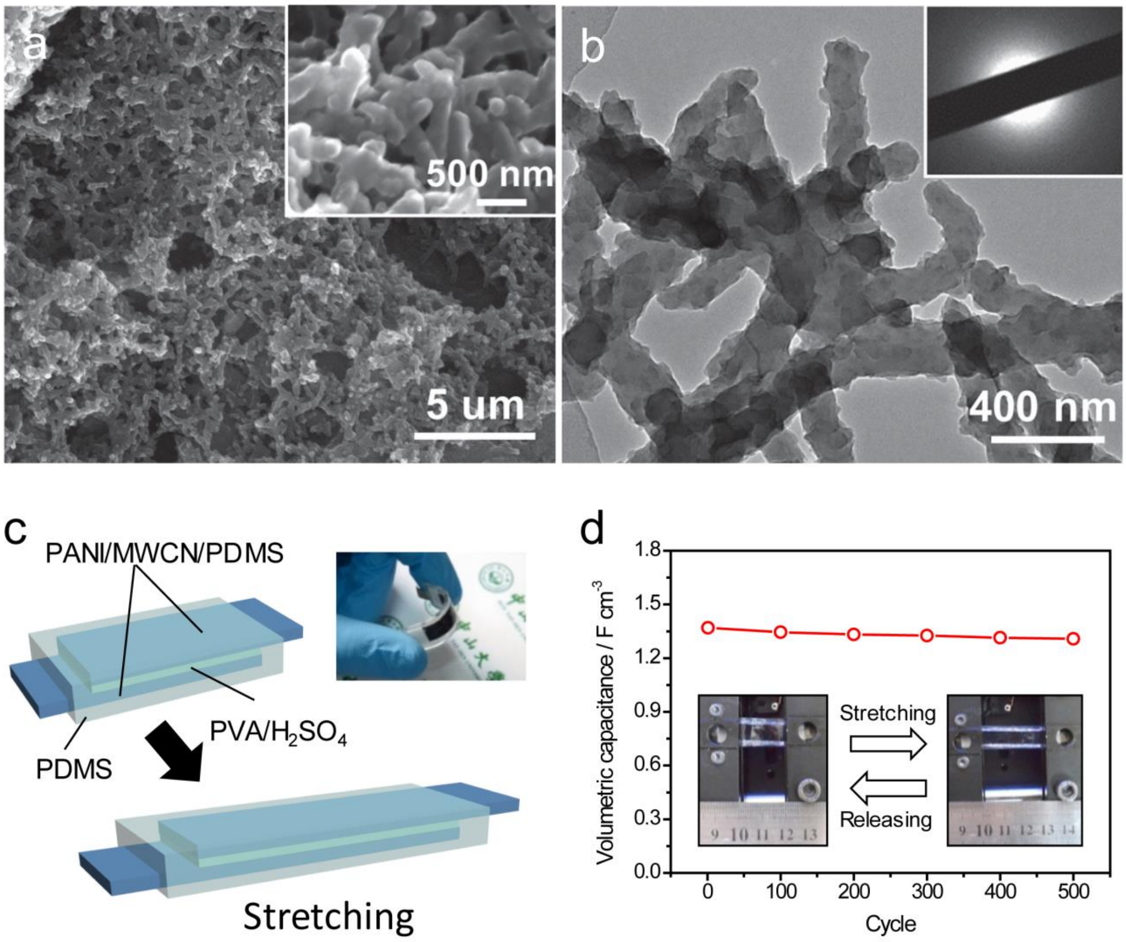

Fig. 25. (a) SEM and (b) TEM of polyaniline nanowires. (c) A schematic diagram of stretchable PANI-SSC. (d) Cycling performance of the PANI-SSC device collected at 10 mV/s under dynamic stretching and releasing condition. Reproduced from Ref. [204] with permission from WILEY-VCH Verlag GmbH & Co. KGaA, Weinheim.

Recently, a large amount of novel electrode materials were investigated as the SC electrode materials, like metal nitride,[210-212] metal sulfide[213, 214] and metal selenium[215]. Although only a few studies were focused on the fabrication of 3D architectures based on these materials, [213, 215-217] it is believed that constructing 3D structure is a developing direction for the further improvement of their electrochemical performance. Similar strategies of metal oxides can be applied for reference, including the self-assembly and multi-step assembly. As a preliminary attempt, 3D hierarchical $GeSe_2$ was self-assembled through a thermal evaporation method by Wang *et al.*,[215] which was constructed by pyramid-like architectures with wire-like or belt-like nanostructures grown epitaxially on them. The electrochemical evaluation revealed an remarkable performance with a large specific capacitance of 300 F/g and a superior cycling stability of 99.3% capacitance retention after 2000 charge/discharge cycles. Table 3 summarizes the mass loading of active materials, conductivity and capacitive performance of the other 3D electrodes.

Table 3. Summarized properties of 3D electrodes based on other materials and their corresponding capacitive performances

Electrode description	Fabrication method	Mass loading	Conductivity	Specific capacitance	Cycling performance	Ref.
V_3S_4/3DG	Nickel foam templating	2.8 mg/cm^2	-	225 F/g at 10 mV/s a	98.3% retention at 100 mV/s for 5000 cycles.	32
V_3S4/3DGH//MnO_2/3DGH quasi-solid device	Nickel foam templating	21 mg/cm^2 for whole device	-	22.2 F/g at 6 mA/cm^2	96.4% retention at 30 mA/cm^2 for 5000 cycles	32
Ni–Co sulfide nanowires	Nickel foam support	~2.5 mg/cm^2	-	2.9 F/cm^2 at 30 mA/cm^2	78.5% retention after 3000 cycles at 2.5 mA/cm^2	51
PANI/MWCNT/PDMS based device	Non-template method		4.19 S/cm	159 F/g at 5 mV/s	95% capacitance retention after 500 cycles	204
3D Micro-Supercapacitor	Non-template method	-	-	45.2 mF/cm^2 at	93.1% retention after 2000 cycles at 1000	206

device based on PANI				0.3 mA/cm^2	mV/s	
PANI+HPCM	Non-template method	26% of the whole electrode weight	0.02S/cm^2	2200 F/gat 0.67 A/g	76% retention after 1200 cycles at various rate	205
PEDOT/PSS-SWNT film	Non-template method	8 mg/cm^2	10-20 S/cm	133 F/g at 0.67A /g	90% retention after 1000 cycles at 1 A/g	208
TiN NWs on carbon cloth	Non-template method	-	-	117.5 F/g at 1.8 A/g	83% retention after 15 000 cycle	210
WON nanowires	Non-template method	167.5 mg/cm^3	-	4.95 F/cm^3 at 12.5 mA/cm^3	93% retention after 100 000 cycles at 0.5 A/cm^3	211
3D Hierarchical $GeSe_2$	Non-template method	-	-		99.3% retention after 2000 cycles at 1 A/g	215

5. Summary and Prospective

Since 3D structure has multifaceted advantages over low-dimensional counterpart[13, 14], constructing electrodes with such frameworks will significantly improve the electrochemical performance in SCs device. To achieve high energy density of SCs, advanced features in 3D structure are preferable, such like interconnectivities, reduced “dead surface”, high utilization of active materials, shorten ionic diffusion and faster electrolyte infiltration. In this review, we summarized the fabrication of 3D electrodes and their corresponding application in SCs energy storage, of which the generalization we believe to be of importance for designing 3D electrode and give insights into future electrode fabrication. Overview of both templated and non-templated 3D electrodes fabrication showed promising application potential. Despite that, research focuses of 3D electrodes are restrained in the field of carbon materials, especially graphene, of which the specific capacitance is too low to meet the demand of high energy density comparable to that of lithium ion batteries. Additionally, template methods required long and costly removal process. Even though templates-derived morphologies are more controllable, those methods remain small-scale production and raise controversies in their industrial applications. Moreover, mechanical strength of 3D electrodes can still hardly satisfy the requirement of commercial flexible devices. As one of advantages that 3D electrodes usually possess, flexibility of the electrodes still lack detailed and statistical researches. With all these unresolved problems, following aspects might attract the attention of researchers in hope of developing 3D electrodes with ultrahigh energy density and power density in SC devices:

1) Current researches have been focusing on carbon materials, especially for graphene foams or aero-gels electrodes. The relatively low capacity of carbon materials might limit the overall energy density of the electrode. However, metal oxides, which have been indispensable in the field of SCs, [6] usually possess high theoretical capacitance. Forming composites between metal oxides and 3D carbon materials should be the mainstream of research in the near future as the 3D conductive backbone effectively transports electrons and unique structure allows fast ion diffusion and electrolyte contact, while metal oxides act as pseudocapacitive reaction sites which provide extra capacitance that can be fully utilized due to the 3D backbone.

2) Mechanical strength has always been one of major concerns for 3D electrodes. Sufficient strength can tolerate external force induced by bending or pressing and even restore from shape change, giving prospects for flexible application. [7] Generally speaking, reinforcements of 3D network in current researches commonly involve the impregnation of elastic polymer like PMMA. [24] The insulating nature of such polymers dramatically impedes the conducting of electron and the polymer infiltration into porous structure wipes out the advantages originally brought by porous structure. Thus, new modifications need to be sought out for fortified strength without sacrificing the integrity of 3D structure.

3) Graphene foam or aero-gel is one of most promising 3D electrodes developed by recent studies, due to its macroporous backbone. [15] Several reports attempt to integrate meso-pores into monolithic macroporous matrices of graphene foams to produce

hierarchical porous 3D electrodes and such structure does possess enhancing effect on electrochemical performance. [73, 74, 89] It has been known that the nano/meso-porosity facilitates electrochemical reaction and ion diffusion into internal region of the 3D electrode matrices. Meanwhile, macro-pores derived from NF or self-assembling enable fast mass transfer to give out quick electrochemical response. That means a hierarchical porous structure might gain some advantages in energy storage with high power and sufficient energy density. [159, 218, 219] On such basis, further investigation might continue on balancing the ratio of macroscopic backbone to microscopic porosity of the graphene foam, in order to produce robust 3D electrodes with maximal utilization of electrochemically active reaction sites.

4) Countless template-derived and non-template electrodes have been developed from various templates and assembling procedures but most of these fabrication procedures require multiple steps and involve expansive starting materials. In templating methods, extra step of template removal further obstructs commercial application. Hence, the further optimization by developing convenient templates or facile synthesis procedure might be of value for future fabrication route toward 3DSC electrodes.

ASSOCIATED CONTENT

Author Contributions

The manuscript was written through contributions of all authors. All authors have given approval to the final version of the manuscript.

Notes

The authors declare no competing financial interest.

Acknowledgements

We acknowledges the financial support of this work received by the Natural Science Foundation of China (21403306, and 21273290), Guangdong Province Natural Science Foundation for Distinguished Young Project (2014A030306048), Foundation for Youth Innovative Talents in Higher Education of Guangdong (2014KQNCX003) and The Research Foundation of IARC-SYSU (201408).

References:

1. X. Wang, X. Lu, B. Liu, D. Chen, Y. Tong and G. Shen, *Adv. Mater.*, 2014, **26**, 4763.
2. J. P. Holdren, *Science*, 2007, **315**, 737.
3. A. N. Menegaki, *Renewable Energy*, 2012, **39**, 30.
4. A. K. Akella, R. P. Saini and M. P. Sharma, *Renewable Energy*, 2009, **34**, 390.
5. M. Winter and R. J. Brodd, *Chem. Rev.*, 2004, **104**, 4245.
6. G. Wang, L. Zhang and J. Zhang, *Chem. Soc. Rev.*, 2012, **41**, 797.
7. X. Lu, M. Yu, G. Wang, Y. Tong and Y. Li, *Energy Environ. Sci.*, 2014, **7**, 2160.

8. L. L. Zhang and X. S. Zhao, *Chem. Soc. Rev.*, 2009, **38**, 2520.

9. K. Naoi, W. Naoi, S. Aoyagi, J. Miyamoto and T. Kamino, *Acc. Chem. Res.*, 2013, **46**, 1075.

10. P. Simon and Y. Gogotsi, *Nat. Mater.*, 2008, **7**, 845.

11. J. R. Miller and P. Simon, *Science*, 2008, **321**, 651.

12. X. Cao, Z. Yin and H. Zhang, *Energy Environ. Sci.*, 2014, **7**, 1850.

13. Y. Zhao, B. Liu, L. Pan and G. Yu, *Energy Environ. Sci.*, 2013, **6**, 2856.

14. H. Jiang, P. S. Lee and C. Li, *Energy Environ. Sci.*, 2013, **6**, 41.

15. S. Nardecchia, D. Carriazo, M. L. Ferrer, M. C. Gutierrez and F. del Monte, *Chem. Soc. Rev.*, 2013, **42**, 794.

16. P. Yang and W. Mai, *Nano Energy*, 2014, **8**, 274.

17. P.-C. Gao, W.-Y. Tsai, B. Daffos, P.-L. Taberna, C. R. Pérez, Y. Gogotsi, P. Simon and F. Favier, *Nano Energy*, 2015, **12**, 197.

18. L. Yu, H. B. Wu and X. W. Lou, *Adv. Mater.*, 2013, **25**, 2296.

19. S. J. Hurst, E. K. Payne, L. Qin and C. A. Mirkin, *Angew Chem. Int. Ed.*, 2006, **45**, 2672.

20. Y. Liu, J. Goebl and Y. Yin, *Chem. Soc. Rev.*, 2013, **42**, 2610.

21. D. Chao, X. Xia, J. Liu, Z. Fan, C. F. Ng, J. Lin, H. Zhang, Z. X. Shen and H. J. Fan, *Adv. Mater.*, 2014, **26**, 5794.

22. H. B. Wu, A. Pan, H. H. Hng and X. W. D. Lou, *Adv. Funct. Mater.*, 2013, **23**, 5669.

23. M. Yu, W. Wang, C. Li, T. Zhai, X. Lu and Y. Tong, *NPG Asia Mater.*, 2014, **6**, e129.

24. Z. Chen, W. Ren, L. Gao, B. Liu, S. Pei and H. M. Cheng, *Nat. Mater.*, 2011, **10**, 424.

25. X. C. Dong, H. Xu, X. W. Wang, Y. X. Huang, M. B. Chan-Park, H. Zhang, L. H. Wang, W. Huang and P. Chen, *ACS Nano*, 2012, **6**, 3206.
26. Y. He, W. Chen, X. Li, Z. Zhang, J. Fu, C. Zhao and E. Xie, *ACS Nano*, 2013, **7**, 174.
27. J. Ji, L. L. Zhang, H. Ji, Y. Li, X. Zhao, X. Bai, X. Fan, F. Zhang and R. S. Ruoff, *ACS Nano*, 2013, **7**, 6237.
28. Y. He, W. Chen, J. Zhou, X. Li, P. Tang, Z. Zhang, J. Fu and E. Xie, *ACS Appl. Mater. Interfaces*, 2014, **6**, 210.
29. X. Yu, B. Lu and Z. Xu, *Adv. Mater.*, 2014, **26**, 1044.
30. T. Maiyalagan, X. Dong, P. Chen and X. Wang, *J. Mater. Chem.*, 2012, **22**, 5286.
31. Y. Wang, C. X. Guo, X. Wang, C. Guan, H. Yang, K. Wang and C. M. Li, *Energy Environ. Sci.*, 2011, **4**, 195.
32. T. Zhai, X. Lu, H. Wang, G. Wang, T. Mathis, T. Liu, C. Li, Y. Tong and Y. Li, *Nano Lett.*, 2015, **15**, 3189.
33. Z. Y. Zhang, F. Xiao, L. H. Qian, J. W. Xiao, S. Wang and Y. Q. Liu, *Adv. Energy Mater.*, 2014, **4**, 1400064.
34. F. Luan, G. Wang, Y. Ling, X. Lu, H. Wang, Y. Tong, X. X. Liu and Y. Li, *Nanoscale*, 2013, **5**, 7984.
35. D. Cai, H. Huang, D. Wang, B. Liu, L. Wang, Y. Liu, Q. Li and T. Wang, *ACS Appl. Mater. Interfaces*, 2014, **6**, 15905.
36. L. Qu, Y. Zhao, A. M. Khan, C. Han, K. M. Hercule, M. Yan, X. Liu, W. Chen, D. Wang, Z. Cai, W. Xu, K. Zhao, X. Zheng and L. Mai, *Nano Lett.*, 2015, **15**, 2037.
37. C. Guan, J. Liu, C. Cheng, H. Li, X. Li, W. Zhou, H. Zhang and H. J. Fan, *Energy*

Environ. Sci., 2011, **4**, 4496.

38. P. Yuan, N. Zhang, D. Zhang, T. Liu, L. Chen, X. Liu, R. Ma and G. Qiu, *Chem. Commun.*, 2014, **50**, 11188.
39. X. Xiong, D. Ding, D. Chen, G. Waller, Y. Bu, Z. Wang and M. Liu, *Nano Energy*, 2015, **11**, 154.
40. S. Cai, D. Zhang, L. Shi, J. Xu, L. Zhang, L. Huang, H. Li and J. Zhang, *Nanoscale*, 2014, **6**, 7346.
41. K. Xu, W. Li, Q. Liu, B. Li, X. Liu, L. An, Z. Chen, R. Zou and J. Hu, *J. Mater. Chem. A*, 2014, **2**, 4795.
42. Y. Chen, B. Qu, L. Hu, Z. Xu, Q. Li and T. Wang, *Nanoscale*, 2013, **5**, 9812.
43. D. Yan, Z. Guo, G. Zhu, Z. Yu, H. Xu and A. Yu, *J. Power Sources*, 2012, **199**, 409.
44. C. Zhou, Y. Zhang, Y. Li and J. Liu, *Nano Lett.*, 2013, **13**, 2078.
45. J. Pu, Z. Wang, K. Wu, N. Yu and E. Sheng, *Phys. Chem. Chem. Phys.*, 2014, **16**, 785.
46. W. Wei, L. Mi, Y. Gao, Z. Zheng, W. Chen and X. Guan, *Chemistry Of Materials*, 2014, **26**, 3418.
47. C. H. Tang, X. Yin and H. Gong, *ACS Appl. Mater. Interfaces*, 2013, **5**, 10574.
48. G. Zhang and X. W. Lou, *Adv. Mater.*, 2013, **25**, 976.
49. C. Yuan, J. Li, L. Hou, X. Zhang, L. Shen and X. W. D. Lou, *Adv. Funct. Mater.*, 2012, **22**, 4592.
50. R. Zou, M. F. Yuen, Z. Zhang, J. Hu and W. Zhang, *J. Mater. Chem. A*, 2015, **3**, 1717.
51. Y. Li, L. Cao, L. Qiao, M. Zhou, Y. Yang, P. Xiao and Y. Zhang, *J. Mater. Chem. A*, 2014, **2**, 6540.

52. A. Lesniak, F. Fenaroli, M. P. Monopoli, C. Åberg, K. A. Dawson and A. Salvati, *ACS Nano*, 2012, **6**, 5845.

53. L. Pan, Q. He, J. Liu, Y. Chen, M. Ma, L. Zhang and J. Shi, *J. Am. Chem. Soc.*, 2012, **134**, 5722.

54. B. T. Zhu, Z. Wang, S. Ding, J. S. Chen and X. W. Lou, *RSC Adv.*, 2011, **1**, 397.

55. K. Nakanishi, M. Tomita and K. Kato, *RSC Adv.*, 2014, **4**, 4732.

56. H. S. Huang, K. H. Chang, N. Suzuki, Y. Yamauchi, C. C. Hu and K. C. Wu, *Small*, 2013, **9**, 2520.

57. X. Huang, K. Qian, J. Yang, J. Zhang, L. Li, C. Yu and D. Zhao, *Adv. Mater.*, 2012, **24**, 4419.

58. K.-J. Hwang, D. W. Cho, J.-W. Lee and C. Im, *New J. Chem.*, 2012, **36**, 2094.

59. Z. Lei, J. Zhang and X. S. Zhao, *J. Mater. Chem.*, 2012, **22**, 153.

60. J. B. Joo, Q. Zhang, I. Lee, M. Dahl, F. Zaera and Y. Yin, *Adv. Funct. Mater.*, 2012, **22**, 166.

61. Y. Meng, D. Gu, F. Zhang, Y. Shi, H. Yang, Z. Li, C. Yu, B. Tu and D. Zhao, *Angew. Chem.*, 2005, **117**, 7215.

62. R. Ryoo, S. H. Joo, M. Kruk and M. Jaroniec, *Adv. Mater.*, 2001, **13**, 677.

63. J. Lee, S. Yoon, S. M. Oh, C. H. Shin and T. Hyeon, *Adv. Mater.*, 2000, **12**, 359.

64. J. Lee, S. Han and T. Hyeon, *J. Mater. Chem.*, 2004, **14**, 478.

65. F. Caruso, R. A. Caruso and H. Möhwald, *Science*, 1998, **282**, 1111.

66. Z. Niu, Z. Yang, Z. Hu, Y. Lu and C. C. Han, *Adv. Funct. Mater.*, 2003, **13**, 949.

67. A. Yu, Y. Wang, E. Barlow and F. Caruso, *Adv. Mater.*, 2005, **17**, 1737.

68. F. Marlow, Muldarisnur, P. Sharifi, R. Brinkmann and C. Mendive, *Angew Chem. Int. Ed.*, 2009, **48**, 6212.

69. J. H. Holtz and S. A. Asher, *Nature*, 1997, **389**, 829.

70. S. Kuai, S. Badilescu, G. Bader, R. Brüning, X. Hu and V. V. Truong, *Adv. Mater.*, 2003, **15**, 73.

71. S. Wong, V. Kitaev and G. A. Ozin, *J. Am. Chem. Soc.*, 2003, **125**, 15589.

72. X. Wen, D. Zhang, L. Shi, T. Yan, H. Wang and J. Zhang, *J. Mater. Chem.*, 2012, **22**, 23835.

73. X. Lu, D. Zheng, T. Zhai, Z. Liu, Y. Huang, S. Xie and Y. Tong, *Energy Environ. Sci.*, 2011, **4**, 2915.

74. Z. S. Wu, Y. Sun, Y. Z. Tan, S. Yang, X. Feng and K. Mullen, *J. Am. Chem. Soc.*, 2012, **134**, 19532.

75. S.-J. Ding, C.-L. Zhang, M. Yang, X.-Z. Qu, Y.-F. Lu and Z.-Z. Yang, *Polymer*, 2006, **47**, 8360.

76. S.-W. Kim, M. Kim, W. Y. Lee and T. Hyeon, *J. Am. Chem. Soc.*, 2002, **124**, 7642.

77. M. Yang, J. Ma, C. Zhang, Z. Yang and Y. Lu, *Angew Chem. Int. Ed.*, 2005, **44**, 6727.

78. M. Zhou, H. B. Wu, J. Bao, L. Liang, X. W. Lou and Y. Xie, *Angew Chem. Int. Ed.*, 2013, **52**, 8579.

79. H.-J. Liu, W.-J. Cui, L.-H. Jin, C.-X. Wang and Y.-Y. Xia, *J. Mater. Chem.*, 2009, **19**, 3661.

80. M. Muller, R. Zentel, T. Maka, S. G. Romanov and C. S. Torres, *Adv. Mater.*, 2000, **12**, 1499.

81. P. N. Bartlett, P. R. Birkin and M. A. Ghanem, *Chem. Commun.*, 2000, 1671.

82. S. K. Karuturi, J. Luo, C. Cheng, L. Liu, L. T. Su, A. I. Tok and H. J. Fan, *Adv. Mater.*, 2012, **24**, 4157.

83. Z. Yang, Z. Yao, G. Li, G. Fang, H. Nie, Z. Liu, X. Zhou, X. a. Chen and S. Huang, *ACS Nano*, 2011, **6**, 205.

84. J. Elias, I. Utke, S. Yoon, M. Bechelany, A. Weidenkaff, J. Michler and L. Philippe, *Electrochimica Acta*, 2013, **110**, 387.

85. B. Hsia, M. S. Kim, L. E. Luna, N. R. Mair, Y. Kim, C. Carraro and R. Maboudian, *ACS Appl. Mater. Interfaces*, 2014, **6**, 18413.

86. Z. Liu, J. Ya, Y. Xin, J. Ma and C. Zhou, *Journal Of Crystal Growth*, 2006, **297**, 223.

87. X. H. Xia, J. P. Tu, J. Zhang, J. Y. Xiang, X. L. Wang and X. B. Zhao, *ACS Appl. Mater. Interfaces*, 2010, **2**, 186.

88. I. Yamaguchi, M. Watanabe, T. Shinagawa, M. Chigane, M. Inaba, A. Tasaka and M. Izaki, *ACS Appl. Mater. Interfaces*, 2009, **1**, 1070.

89. B. G. Choi, M. Yang, W. H. Hong, J. W. Choi and Y. S. Huh, *ACS Nano*, 2012, **6**, 4020.

90. L. E. Kreno, K. Leong, O. K. Farha, M. Allendorf, R. P. Van Duyne and J. T. Hupp, *Chem. Rev.*, 2012, **112**, 1105.

91. J. Lee, O. K. Farha, J. Roberts, K. A. Scheidt, S. T. Nguyen and J. T. Hupp, *Chem. Soc. Rev.*, 2009, **38**, 1450.

92. S.-L. Li and Q. Xu, *Energy Environ. Sci.*, 2013, **6**, 1656.

93. K. M. Choi, H. M. Jeong, J. H. Park, Y.-B. Zhang, J. K. Kang and O. M. Yaghi, *ACS Nano*, 2014, **8**, 7451.

94. J. Yang, C. Zheng, P. Xiong, Y. Li and M. Wei, *J. Mater. Chem. A*, 2014, **2**, 19005.

95. R. D íaz, M. G. Orcajo, J. A. Botas, G. Calleja and J. Palma, *Materials Letters*, 2012, **68**, 126.

96. B. Liu, H. Shioyama, T. Akita and Q. Xu, *J. Am. Chem. Soc.*, 2008, **130**, 5390.

97. H. Wang, Q. Gao and J. Hu, *J. Power Sources*, 2010, **195**, 3017.

98. D. Yuan, J. Chen, S. Tan, N. Xia and Y. Liu, *Electrochemistry Communications*, 2009, **11**, 1191.

99. W. Chaikittisilp, M. Hu, H. Wang, H. S. Huang, T. Fujita, K. C. Wu, L. C. Chen, Y. Yamauchi and K. Ariga, *Chem. Commun.*, 2012, **48**, 7259.

100. A. J. Amali, J. K. Sun and Q. Xu, *Chem. Commun.*, 2014, **50**, 1519.

101. B. Liu, H. Shioyama, H. Jiang, X. Zhang and Q. Xu, *Carbon*, 2010, **48**, 456.

102. J. Hu, H. Wang, Q. Gao and H. Guo, *Carbon*, 2010, **48**, 3599.

103. X. Liu, L. Zhou, Y. Zhao, L. Bian, X. Feng and Q. Pu, *ACS Appl. Mater. Interfaces*, 2013, **5**, 10280.

104. W. Xia, B. Qiu, D. Xia and R. Zou, *Sci. Rep.*, 2013, **3**, 1935.

105. X. Lang, A. Hirata, T. Fujita and M. Chen, *Nature Nanotechnology*, 2011, **6**, 232.

106. X. Lang, L. Zhang, T. Fujita, Y. Ding and M. Chen, *J. Power Sources*, 2012, **197**, 325.

107. N. Liu, W. Ma, J. Tao, X. Zhang, J. Su, L. Li, C. Yang, Y. Gao, D. Golberg and Y. Bando, *Adv. Mater.*, 2013, **25**, 4925.

108. H. Pang, S. J. Ee, Y. Dong, X. Dong and P. Chen, *ChemElectroChem*, 2014, **1**, 1027.

109. W. He, C. Jiang, J. Wang and L. Lu, *Angew Chem. Int. Ed.*, 2014, **53**, 9503.

110. Y. Meng, K. Wang, Y. Zhang and Z. Wei, *Adv. Mater.*, 2013, **25**, 6985.

111. K. S. Novoselov, A. K. Geim, S. V. Morozov, D. Jiang, Y. Zhang, S. V. Dubonos, I. V. Grigorieva and A. A. Firsov, *Science*, 2004, **306**, 666.

112. M. J. Allen, V. C. Tung and R. B. Kaner, *Chem. Rev.*, 2009, **110**, 132.

113. W. S. Hummers and R. E. Offeman, *J. Am. Chem. Soc.*, 1958, **80**, 1339.

114. J. Yan, J. Liu, Z. Fan, T. Wei and L. Zhang, *Carbon*, 2012, **50**, 2179.

115. Y. Yoon, K. Lee, C. Baik, H. Yoo, M. Min, Y. Park, S. M. Lee and H. Lee, *Adv. Mater.*, 2013, **25**, 4437.

116. Z. Wen, X. Wang, S. Mao, Z. Bo, H. Kim, S. Cui, G. Lu, X. Feng and J. Chen, *Adv. Mater.*, 2012, **24**, 5610.

117. J. Luo, H. D. Jang and J. Huang, *ACS Nano*, 2013, **7**, 1464.

118. T. Kim, G. Jung, S. Yoo, K. S. Suh and R. S. Ruoff, *ACS Nano*, 2013, **7**, 6899.

119. Y. Xu, K. Sheng, C. Li and G. Shi, *ACS Nano*, 2010, **4**, 4324.

120. Z. S. Wu, A. Winter, L. Chen, Y. Sun, A. Turchanin, X. Feng and K. Mullen, *Adv. Mater.*, 2012, **24**, 5130.

121. Z. Chen, Y. Qin, D. Weng, Q. Xiao, Y. Peng, X. Wang, H. Li, F. Wei and Y. Lu, *Adv. Funct. Mater.*, 2009, **19**, 3420.

122. J. Liang, Y. Jiao, M. Jaroniec and S. Z. Qiao, *Angew Chem. Int. Ed.*, 2012, **51**, 11496.

123. C. Zhang, N. Mahmood, H. Yin, F. Liu and Y. Hou, *Adv. Mater.*, 2013, **25**, 4932.

124. S. Some, J. Kim, K. Lee, A. Kulkarni, Y. Yoon, S. Lee, T. Kim and H. Lee, *Adv. Mater.*, 2012, **24**, 5481.

125. T. Martins, R. Miwa, A. J. da Silva and A. Fazzio, *Physical Review Letters*, 2007, **98**, 196803.

126. X. Xie, C. Zhang, M. B. Wu, Y. Tao, W. Lv and Q. H. Yang, *Chem. Commun.*, 2013, **49**, 11092.

127. D. A. Dikin, S. Stankovich, E. J. Zimney, R. D. Piner, G. H. Dommett, G. Evmenenko, S. T. Nguyen and R. S. Ruoff, *Nature*, 2007, **448**, 457.

128. H. Chen, M. B. Müller, K. J. Gilmore, G. G. Wallace and D. Li, *Adv. Mater.*, 2008, **20**, 3557.

129. X. Yang, J. Zhu, L. Qiu and D. Li, *Adv. Mater.*, 2011, **23**, 2833.

130. X. Yang, C. Cheng, Y. Wang, L. Qiu and D. Li, *Science*, 2013, **341**, 534.

131. Z. Fan, J. Yan, L. Zhi, Q. Zhang, T. Wei, J. Feng, M. Zhang, W. Qian and F. Wei, *Adv. Mater.*, 2010, **22**, 3723.

132. F. Du, D. Yu, L. Dai, S. Ganguli, V. Varshney and A. K. Roy, *Chemistry Of Materials*, 2011, **23**, 4810.

133. B. You, L. Wang, L. Yao and J. Yang, *Chem. Commun.*, 2013, **49**, 5016.

134. X. Cao, B. Zheng, X. Rui, W. Shi, Q. Yan and H. Zhang, *Angew Chem. Int. Ed.*, 2014, **53**, 1404.

135. Y. Shao, H. Wang, Q. Zhang and Y. Li, *J. Mater. Chem. C*, 2013, **1**, 1245.

136. Y. G. Zhu, Y. Wang, Y. M. Shi, Z. X. Huang, L. Fu and H. Y. Yang, *Adv. Energy Mater.*, 2014, **4**, 1301788.

137. S. Wu, W. Chen and L. Yan, *J. Mater. Chem. A*, 2014, **2**, 2765.

138. H. Wang, H. Yi, X. Chen and X. Wang, *J. Mater. Chem. A*, 2014, **2**, 1165.

139. L. Zhang, F. Zhang, X. Yang, G. Long, Y. Wu, T. Zhang, K. Leng, Y. Huang, Y. Ma, A. Yu and Y. Chen, *Sci. Rep.*, 2013, **3**, 1408.

140. Y. Gong, S. Yang, L. Zhan, L. Ma, R. Vajtai and P. M. Ajayan, *Adv. Funct. Mater.*, 2014, **24**, 125.

141.M. Yu, Y. Huang, C. Li, Y. Zeng, W. Wang, Y. Li, P. Fang, X. Lu and Y. Tong, *Adv. Funct. Mater.*, 2015, **25**, 324.

142. U. N. Maiti, J. Lim, K. E. Lee, W. J. Lee and S. O. Kim, *Adv. Mater.*, 2014, **26**, 615.

143. M. F. El-Kady, V. Strong, S. Dubin and R. B. Kaner, *Science*, 2012, **335**, 1326.

144. Z. Niu, J. Chen, H. H. Hng, J. Ma and X. Chen, *Adv. Mater.*, 2012, **24**, 4144.

145. S. Iijima, *Nature*, **354**, 56.

146. R. R. Kohlmeyer, M. Lor, J. Deng, H. Liu and J. Chen, *Carbon*, 2011, **49**, 2352.

147. Z. Chen, V. Augustyn, X. Jia, Q. Xiao, B. Dunn and Y. Lu, *ACS Nano*, 2012, **6**, 4319.

148. Z. Chen, V. Augustyn, J. Wen, Y. Zhang, M. Shen, B. Dunn and Y. Lu, *Adv. Mater.*, 2011, **23**, 791.

149. X. Zhang, W. Shi, J. Zhu, D. J. Kharistal, W. Zhao, B. S. Lalia, H. H. Hng and Q. Yan, *ACS Nano*, 2011, **5**, 2013.

150. L. Zhang, C. M. B. Holt, E. J. Luber, B. C. Olsen, H. Wang, M. Danaie, X. Cui, X. Tan, V. W. Lui, W. P. Kalisvaart and D. Mitlin, *J. Phys. Chem. C*, 2011, **115**, 24381.

151. D. Wei, H. Wang, P. Hiralal, P. Andrew, T. Ryhanen, Y. Hayashi and G. A. Amaratunga, *Nanotechnology*, 2010, **21**, 435702.

152. A. B. Deshmukh and M. V. Shelke, *RSC Adv.*, 2013, **3**, 21390.

153. C. M. Yang, Y. J. Kim, M. Endo, H. Kanoh, M. Yudasaka, S. Iijima and K. Kaneko, *J. Am. Chem. Soc.*, 2007, **129**, 20.

154. T. Azami, D. Kasuya, R. Yuge, M. Yudasaka, S. Iijima, T. Yoshitake and Y. Kubo, *J.*

Phys. Chem. C, 2008, **112**, 1330.

155. H. J. Jung, Y.-J. Kim, J. H. Han, M. Yudasaka, S. Iijima, H. Kanoh, Y. A. Kim, K. Kaneko and C.-M. Yang, *J. Phys. Chem. C*, 2013, **117**, 25877.
156. A. Izadi-Najafabadi, T. Yamada, D. N. Futaba, M. Yudasaka, H. Takagi, H. Hatori, S. Iijima and K. Hata, *ACS Nano*, 2011, **5**, 811.
157. C. Peng, Z. Wen, Y. Qin, L. Schmidt‐Mende, C. Li, S. Yang, D. Shi and J. Yang, *ChemSusChem*, 2014, **7**, 777.
158. G. Xu, B. Ding, P. Nie, L. Shen, J. Wang and X. Zhang, *Chem. Eur. J.*, 2013, **19**, 12306.
159. D.-W. Wang, F. Li, M. Liu, G. Q. Lu and H.-M. Cheng, *Angew. Chem.*, 2008, **120**, 379.
160. W. Chen and L. Yan, *Nanoscale*, 2011, **3**, 3132.
161. J. Li, X. Wang, Q. Huang, S. Gamboa and P. J. Sebastian, *J. Power Sources*, 2006, **158**, 784.
162. J. Li, X. Wang, Q. Huang, S. Gamboa and P. J. Sebastian, *J. Power Sources*, 2006, **160**, 1501.
163. S.-W. Hwang and S.-H. Hyun, *J. Power Sources*, 2007, **172**, 451.
164. H. An, Y. Wang, X. Wang, L. Zheng, X. Wang, L. Yi, L. Bai and X. Zhang, *J. Power Sources*, 2010, **195**, 6964.
165. H.-C. Chien, W.-Y. Cheng, Y.-H. Wang and S.-Y. Lu, *Adv. Funct. Mater.*, 2012, **22**, 5038.
166. Y.-H. Lin, T.-Y. Wei, H.-C. Chien and S.-Y. Lu, *Adv. Energy Mater.*, 2011, **1**, 901.
167. J. M. Miller and B. Dunn, *Langmuir*, 1999, **15**, 799.
168. M. C. Gutiérrez, F. Picó, F. Rubio, J. Manuel Amarilla, F. Javier Palomares, M. L. Ferrer, F. del Monte and J. M. Rojo, *J. Mater. Chem.*, 2009, **19**, 1236.

169. M. Biswal, A. Banerjee, M. Deo and S. Ogale, *Energy Environ. Sci.*, 2013, **6**, 1249.

170. Y. Lv, L. Gan, M. Liu, W. Xiong, Z. Xu, D. Zhu and D. S. Wright, *J. Power Sources*, 2012, **209**, 152.

171. Y. S. Yun, S. Y. Cho, J. Shim, B. H. Kim, S. J. Chang, S. J. Baek, Y. S. Huh, Y. Tak, Y. W. Park, S. Park and H. J. Jin, *Adv. Mater.*, 2013, **25**, 1993.

172. X. He, P. Ling, M. Yu, X. Wang, X. Zhang and M. Zheng, *Electrochimica Acta*, 2013, **105**, 635.

173. H. Jin, X. Wang, Y. Shen and Z. Gu, *J. Anal. Appl. Pyrol.*, 2014, **110**, 18.

174. M. Genovese, J. Jiang, K. Lian and N. Holm, *J. Mater. Chem. A*, 2015, **3**, 2903.

175. D. Kalpana, S. H. Cho, S. B. Lee, Y. S. Lee, R. Misra and N. G. Renganathan, *J. Power Sources*, 2009, **190**, 587.

176. M.-C. Liu, L.-B. Kong, C. Lu, X.-M. Li, Y.-C. Luo and L. Kang, *RSC Adv.*, 2012, **2**, 1890.

177. Z. Lei, N. Christov and X. S. Zhao, *Energy Environ. Sci.*, 2011, **4**, 1866.

178. Z. Chen, J. Wen, C. Yan, L. Rice, H. Sohn, M. Shen, M. Cai, B. Dunn and Y. Lu, *Adv. Energy Mater.*, 2011, **1**, 551.

179. M. Yu, T. Zhai, X. Lu, X. Chen, S. Xie, W. Li, C. Liang, W. Zhao, L. Zhang and Y. Tong, *J. Power Sources*, 2013, **239**, 64.

180. K. Liang, X. Tang and W. Hu, *J. Mater. Chem.*, 2012, **22**, 11062.

181. X. Xia, J. Tu, Y. Zhang, X. Wang, C. Gu, X. B. Zhao and H. J. Fan, *ACS Nano*, 2012, **6**, 5531.

182. F. Zhang, C. Yuan, J. Zhu, J. Wang, X. Zhang and X. W. D. Lou, *Adv. Funct. Mater.*,

2013, **23**, 3909.

183. X. Xia, D. Chao, Z. Fan, C. Guan, X. Cao, H. Zhang and H. J. Fan, *Nano Lett.*, 2014, **14**, 1651.

184. C. Guan, Z. Zeng, X. Li, X. Cao, Y. Fan, X. Xia, G. Pan, H. Zhang and H. J. Fan, *Small*, 2014, **10**, 300.

185. G. Wang, X. Lu, Y. Ling, T. Zhai, H. Wang, Y. Tong and Y. Li, *ACS Nano*, 2012, **6**, 10296.

186. T. Zhai, X. Lu, Y. Ling, M. Yu, G. Wang, T. Liu, C. Liang, Y. Tong and Y. Li, *Adv. Mater.*, 2014, **26**, 5869.

187. X. Lu, Y. Zeng, M. Yu, T. Zhai, C. Liang, S. Xie, M. S. Balogun and Y. Tong, *Adv. Mater.*, 2014, **26**, 3148.

188. H. Jiang, J. Ma and C. Li, *Adv. Mater.*, 2012, **24**, 4197.

189. J. Zhu, L. Cao, Y. Wu, Y. Gong, Z. Liu, H. E. Hoster, Y. Zhang, S. Zhang, S. Yang, Q. Yan, P. M. Ajayan and R. Vajtai, *Nano Lett.*, 2013, **13**, 5408.

190. C.-M. Huang, C.-C. Hu, K.-H. Chang, J.-M. Li and Y.-F. Li, *Journal Of The Electrochemical Society*, 2009, **156**, A667.

191. Y. Ren and L. Gao, *J. Am. Chem. Soc.*, 2010, **93**, 3560.

192. Y.-T. Wang, A.-H. Lu, H.-L. Zhang and W.-C. Li, *J. Phys. Chem. C*, 2011, **115**, 5413.

193. P. Yu, X. Zhang, D. Wang, L. Wang and Y. Ma, *Crystal Growth & Design*, 2009, **9**, 528.

194. W. Chen, R. B. Rakhi, Q. Wang, M. N. Hedhili and H. N. Alshareef, *Adv. Funct. Mater.*, 2014, **24**, 3130.

195. Y. Wang, Y. Lei, J. Li, L. Gu, H. Yuan and D. Xiao, *ACS Appl. Mater. Interfaces*, 2014, **6**,

6739.

196. Y. Lei, J. Li, Y. Wang, L. Gu, Y. Chang, H. Yuan and D. Xiao, *ACS Appl. Mater. Interfaces*, 2014, **6**, 1773.

197. X. Sun, Q. Li, Y. Lu and Y. Mao, *Chem. Commun.*, 2013, **49**, 4456.

198. J. Liu, J. Jiang, M. Bosman and H. J. Fan, *J. Mater. Chem.*, 2012, **22**, 2419.

199. J. Liu, J. Jiang, C. Cheng, H. Li, J. Zhang, H. Gong and H. J. Fan, *Adv. Mater.*, 2011, **23**, 2076.

200. J. Yan, A. Sumboja, E. Khoo and P. S. Lee, *Adv. Mater.*, 2011, **23**, 746.

201. H. Wu, M. Xu, Y. Wang and G. Zheng, *Nano Res.*, 2013, **6**, 167.

202. Z. Yu and J. Thomas, *Adv. Mater.*, 2014, **26**, 4279.

203. L. Q. Mai, F. Yang, Y. L. Zhao, X. Xu, L. Xu and Y. Z. Luo, *Nature Communications*, 2011, **2**, 381.

204. M. Yu, Y. Zhang, Y. Zeng, M. S. Balogun, K. Mai, Z. Zhang, X. Lu and Y. Tong, *Adv. Mater.*, 2014, **26**, 4724.

205. L. Z. Fan, Y. S. Hu, J. Maier, P. Adelhelm, B. Smarsly and M. Antonietti, *Adv. Funct. Mater.*, 2007, **17**, 3083.

206. C. Z. Meng, J. Maeng, S. W. M. John and P. P. Irazoqui, *Adv. Energy Mater.*, 2014, **4**, 1301269.

207. R. K. Sharma, A. C. Rastogi and S. B. Desu, *Electrochemistry Communications*, 2008, **10**, 268.

208. D. Antiohos, G. Folkes, P. Sherrell, S. Ashraf, G. G. Wallace, P. Aitchison, A. T. Harris, J. Chen and A. I. Minett, *J. Mater. Chem.*, 2011, **21**, 15987.

209. A. K. Cuentas Gallegos and M. E. Rincón, *J. Power Sources*, 2006, **162**, 743.

210. X. Lu, G. Wang, T. Zhai, M. Yu, S. Xie, Y. Ling, C. Liang, Y. Tong and Y. Li, *Nano Lett.*, 2012, **12**, 5376.

211. M. Yu, Y. Han, X. Cheng, L. Hu, Y. Zeng, M. Chen, F. Cheng, X. Lu and Y. Tong, *Adv. Mater.*, 2015, **27**, 3085.

212. M.-S. Balogun, W. Qiu, W. Wang, P. Fang, X. Lu and Y. Tong, *J. Mater. Chem. A*, 2015, **3**, 1364.

213.X. Xia, C. Zhu, J. Luo, Z. Zeng, C. Guan, C. F. Ng, H. Zhang and H. J. Fan, *Small*, 2014, **10**, 766.

214. J. Xiao, L. Wan, S. Yang, F. Xiao and S. Wang, *Nano Lett.*, 2014, **14**, 831.

215. X. Wang, B. Liu, Q. Wang, W. Song, X. Hou, D. Chen, Y. B. Cheng and G. Shen, *Adv. Mater.*, 2013, **25**, 1479.

216. P. P. Wang, H. Sun, Y. Ji, W. Li and X. Wang, *Adv. Mater.*, 2014, **26**, 964.

217. Q. Wang, L. Jiao, H. Du, J. Yang, Q. Huan, W. Peng, Y. Si, Y. Wang and H. Yuan, *CrystEngComm*, 2011, **13**, 6960.

218. J. Liu, S. Z. Qiao, S. Budi Hartono and G. Q. Lu, *Angew. Chem.*, 2010, **122**, 5101.

219. C. Yuan, X. Zhang, L. Su, B. Gao and L. Shen, *J. Mater. Chem.*, 2009, **19**, 5772.

Currently, three-dimensional (3D) nanostructured electrodes have been a new hot topic for the fabrication of high-performance supercapacitors due to their advanced features, such like reduced “dead surface”, good electron transport kinetics, hierarchical porous channels and short ionic diffusion distances. This review presents the current progress of 3D structured electrodes, mainly focusing on their design, assembly and applications in supercapacitors. The main challenges and new trends in 3D electrodes development have also been proposed.